SUPPLEMENTARY INFORMATION APPENDIX: Cation-induced kinetic heterogeneity of the intron-exon recognition in single group II introns

SUPPLEMENTARY METHODS

All chemicals used for the preparation of buffers and stock solutions were at least *puriss p.a.* and were purchased from Sigma-Aldrich AG (Buchs, Switzerland). Buffers and solutions were prepared using double-distilled autoclaved water (ddH_2O) and were subjected to additional filtering using 0.2 µm syringe filters immediately prior to use.

Mass spectrometry. RNA was desalted using a Ziptip (Millipore, Molsheim, France) according to the instructions of the manufacturer. Samples were measured at continuous flow at 3 µL/min. The mass spectrometer Bruker MaXis (Bruker AG, Fällanden, Switzerland) was operated in the negative electrospray ionization mode at 3,000 V (IBS1*) or 5000 V (d3'EBS1*) capillary voltage, –500 V endplate offset, with a N_2 nebulizer pressure of 0.4 bar and dry gas flow of 4 L min^{-1} at 180 °C. MS acquisitions were performed in the mass range from *m*/*z* 50 to 5'000 at 20'000 resolution (full width at half maximum) and 1.0 Hz spectra rate. Data processing was performed in Compass DataAnalysis 4.2 (Bruker Daltonics, Fällanden, Switzerland) and spectra were deconvoluted using the maximum entropy algorithm. Protocol adapted from ref. (1).

Native gel electrophoresis. 20 pmol Cy3-d3'EBS1*-biotin and an increasing quantity of Cy5-IBS1* (0.25 to 5 equivalents) dissolved in 10 µL running buffer (5 mM MOPS, 2 mM NaOH, 50 µM $MgCl_2$ or 50 µM $CaCl_2$, pH 6.90) were loaded onto a polyacrylamide gel (18% w/v acrylamide/bis-acrylamide, dissolved in running buffer). The gel was run at 4 °C in running buffer until the fragments had migrated to the lower half of the gel. The resulting bands were recorded with a Typhoon 9410 multipurpose scanner (GE Healthcare, Glattbrugg, Switzerland).

UV melting experiments. Temperature dependent absorption was recorded at 260 nm on a Cary 500 Scan UV-Vis spectrophotometer (Varian Inc., Palo Alto, USA) equipped with a Cary Temperature Controller in quartz cuvettes with 1 cm path length (Hellma GmbH & Co. KG, Müllheim, Germany). Samples contained 3 µM Cy3-d3'EBS1*-biotin/Cy5-IBS1* dissolved in standard buffer degassed and overlaid with paraffin oil prior to measurements (Table S5). Absorption was monitored in a temperature range of 80-10 °C at a temperature changing rate of 0.5 °C/min, followed by van't Hoff analysis as described (2, 3).

Bulk fluorescence control experiments. Bulk fluorescence experiments were performed with a Safire 2 microplate reader (Tecan Group Ltd., Männedorf, Switzerland). 3995-COR 96-well plates (Vitaris, Baar, Switzerland) display minimal autofluorescence and crosstalk and are coated to prevent surface attachment of the sample. Samples contained sulfonated cyanine dye NHS esters (Cy3 or Cy5, GE Healthcare, Glattbrugg, Switzerland) or sulfonated cyanine dyes tagged to RNA (d3'EBS1* or IBS1*) dissolved in reaction buffer at a consistent concentration of 100 nM (Table S5). The sample also contained 0, 1, 10, 100 or 1000 mM $Mg(NO_3)_2$ or $Ca(NO_3)_2$. Each measurement was repeated using three independent samples to calculate the standard deviation. MilliQ ddH_2O, 1x OSS in MilliQ H_2O, as well as reaction buffer with and without OSS were also measured to determine the contributions of individual compounds to the background noise.

Fluorescence intensities were quantified performing fixed wavelength scans at constant equal slit width and $\lambda_{exc/em}$ = 530/560 nm for Cy3 and $\lambda_{exc/em}$ = 600/660 nm for Cy5, respectively. Fluorescence spectra were recorded, averaged and smoothed with a sliding average filter using a window of 10 data points (4), followed by normalization to 1. Anisotropy (r) was quantified as

$$r = \frac{I_{\parallel} - I_{\perp}}{I_{\parallel} - 2I_{\perp}}$$

where $I_{\parallel}$ and $I_{\perp}$ refer to the emission intensities when the emission polarizer is parallel or perpendicular relative to the direction of polarized excitation (5).

Single molecule FRET experiments. d3'EBS1* was immobilized within a self-built microfluidic channel using a biotin-streptavidin linker according to a protocol modified from (6) and (7) (for a description of the buffers and solution please refer to Table S5): The chamber was flushed with 200 µL T50 buffer to remove impurities from the surface, followed by the injection of 50 µL BSA-biotin solution, and incubation for 10 minutes. Then, the channel was flushed with 200 µl T50 buffer and 50 µL streptavidin solution, followed by 5 minutes incubation. Excess streptavidin was removed by washing with 100 µL standard buffer and the channel was flushed with 80 µL d3'EBS1* solution and incubated for 5 minutes. Finally, 200 µL reaction buffer containing IBS1*, an enzymatic oxygen scavenger solution (OSS; glucose oxidase: Sigma-Aldrich AG, Steinheim, Germany; catalase: Thermo Scientific, Rockford, IL, USA) to reduce photobleaching as well as 1 mM Trolox to suppress dye blinking were added and measurements were started (8, 9). All smFRET experiments were performed at room temperature upon excitation at 532 nm. Both donor and acceptor emission intensities were monitored over 400 seconds using a total internal reflection fluorescence (TIRF)

microscope equipped with a charge-coupled device (10 frames/s, 4000 frames) (6, 7).

Movie processing and data analysis. Single fluorophore emission time traces were manually selected for anticorrelated donor/acceptor emission using a home-written software. Single-molecule clips were imported, followed by identification of single-fluorophore emission, co-localization of the corresponding donor and the acceptor coordinates and creation of time traces. The resulting raw time traces were corrected for background noise using an aperture photometry approach, photo-bleaching, leakage of donor emission into the acceptor channel and direct acceptor excitation (10, 11). Smoothing was performed in the absence of short dwell times in the docked/undocked state using a non-linear forward-backward filter (12, 13). Corrected donor and acceptor emission intensities, I_D and I_A, were used to calculate the apparent FRET efficiency as described (14):

$$FRET = \frac{I_A^D}{I_D^D + I_A^D} \quad (1)$$

For each buffer condition, more than 250 *apparent FRET efficiency* time traces of 400 seconds observation time matching the selection criteria were evaluated and categorized into the following subgroups (15):

- Type I: molecules undergoing at least two transitions, referred to as dynamic molecules.
- Type II: molecules undergoing one transition.
- Type III: molecules undergoing no transition, referred to as static molecules.
    - Type IIIa: molecules remaining in the zero *FRET* state.
    - Type IIIb: molecules remaining in the high *FRET* state.

Cross-sample variability was estimated via bootstrapping using the freely available software package BOBA FRET (16).

Single-molecule control experiments. Alternating laser excitation (ALEX) at 532 nm and 640 nm was performed using mechanical shutters synchronized with the CCD read-out as described (11). This extension yields an additional photon count over time, *i.e.* FRET acceptor intensity upon direct acceptor excitation, which allows to calculate the *stoichiometry of fluorophores* and the detection of photophysical artifacts (17-19).

$$stoichiometry = \frac{I_{\mathrm{D}}^{\mathrm{D}} + I_{\mathrm{A}}^{\mathrm{D}}}{I_{\mathrm{D}}^{\mathrm{D}} + I_{\mathrm{A}}^{\mathrm{D}} + I_{\mathrm{A}}^{\mathrm{A}}} \quad (2)$$

ALEX-experiments involved direct immobilization of single d'EBS1* molecules on a BSA-coated surface (*vide supra*), as well as indirect immobilization of d3'EBS1* and IBS1* via surface-tethered lipid vesicles. For vesicle encapsulation, 1.6 µM/strand RNA were co-encapsulated in phospholipid vesicles (Ø = 100 nm,100:1 DMPC/biotin-PE in standard buffer containing 50 mM $MgCl_2$, Table S5) as described (20). Vesicle suspensions at a lipid concentration of 50 mg mL^{-1} of lipid were diluted in standard buffer for subsequent immobilization on a quartz slide passivated with biotinylated BSA. smFRET measurements were performed at using ALEX in reaction buffer at a $MgCl_2$ concentration of 50 mM (Table S5). In order to rule out encapsulation of multiple d3'EBS1*/IBS1* molecules, dyes were photobleached at the end of the experiment using a laser power of about 20 mW for both excitation at 532 nm and 640 nm.

Additionally, the influence of Mg^{2+} and Ca^{2+} on the photophysics of Cy3 and Cy5 was characterized. For this purpose, Cy3-d3'EBS1* or Cy5-d3'EBS1* were surface-immobilized as described above, followed by monitoring $I_{\mathrm{D}}^{\mathrm{D}}$ and $I_{\mathrm{A}}^{\mathrm{A}}$ at 0, 1, 10, or 100 mM Mg^{2+}/Ca^{2+} over 400 seconds. Care was taken to reach photon counts similar to the intensity levels observed in smFRET experiments. Subsequently, photostability, fluorophore bleaching, blinking, and the occurrence of long-lived dark states were quantified as described (21).

Association constants and Gibbs Free Energy. Association and dissociation constants (K_A, K_D) were determined either from the binned apparent FRET efficiency histograms according to Eq. 3 or by analysis of dwell-times in the docked/undocked state according to Eq. 4. The latter were obtained by thresholding as described (16, 22).

$$K_{\mathrm{A}} = \frac{1}{K_{\mathrm{D}}} = \frac{c(\mathrm{DA})}{c(\mathrm{D})c(\mathrm{A})} = \frac{c(\mathrm{d3'EBS1^*/IBS1^*})}{c(\mathrm{d3'EBS1^*})c(\mathrm{IBS1^*})} \cong \frac{p\left(FRET_{\mathrm{high}}\right)}{p(FRET_{\mathrm{zero}})c_{\mathrm{total}}(\mathrm{IBS1^*})} \quad (3)$$

$$K_{\mathrm{A}} = \frac{1}{K_{\mathrm{D}}} \cong \frac{1 - \frac{t_{\mathrm{zero}}}{t_{\mathrm{zero}}+t_{\mathrm{high}}}}{\frac{t_{\mathrm{zero}}}{t_{\mathrm{zero}}+t_{\mathrm{high}}} c(\mathrm{IBS1^*})} \cong \frac{t_{\mathrm{high}}}{t_{\mathrm{zero}} c_{\mathrm{total}}(\mathrm{IBS1^*})} \quad (4)$$

c(D), c(A), and c(DA) are the absolute concentrations of undocked FRET donor D, free FRET acceptor A, and donor-acceptor complex in the docked state DA. The relative population of docked

and undocked d3'EBS1* molecules (c(d3'EBS1*/IBS1*) and c(d3'EBS1*)) was determined from the binned *apparent FRET efficiency* histograms $p(FRET)$ shown in Figs. S5 and S6. $p(FRET_{\mathrm{high}})$ are the cumulative counts with $FRET > 0.375$, $p\left(FRET_{\mathrm{high}}\right) = \int_{0.375}^{1.2} p(FRET)\, dFRET$, corresponding to the docked species. The population of undocked species $p(FRET_{\mathrm{zero}})$ is defined as $FRET < 0.375$, with $p(FRET_{\mathrm{zero}}) = \int_{-0.2}^{0.375} p(FRET) dFRET$. The undocked fraction $P(<0.375)$ is thus defined as the ratio of undocked molecules and the sum of docked and undocked molecules:

$$\frac{t_{\mathrm{undocked}}}{t_{\mathrm{undocked}} + t_{\mathrm{docked}}} = \frac{t_{\mathrm{zero}}}{t_{\mathrm{zero}} + t_{\mathrm{high}}} = \frac{\int_{-0.2}^{0.375} p(FRET) dFRET}{\int_{-0.2}^{0.375} p(FRET) dFRET + \int_{0.375}^{1.2} p(FRET) dFRET} = P(< 0.375) \quad (5a)$$

Analogously, the docked fraction $P(>0.375)$ is defined as $1 - P(<0.375)$. Integration of the cumulated *FRET* histograms $p(FRET)$ and normalization to 1 yields the cumulative probability distribution P (4). t_{zero} and t_{high} are the dwell times in the zero and high *FRET* state observed under a given buffer condition. The concentration of undocked IBS1* c(IBS1*) is approximated by the total concentration c_{total}(IBS1*), assuming that c_{total}(IBS1*) >> c(d3'EBS1*).

The association constant of an individual molecule n $K_{A,n}$ was determined according to Eq. 5b:

$$K_{\mathrm{A},n} = \frac{1}{K_{\mathrm{D},n}} \cong \frac{\langle t_{\mathrm{high},n} \rangle}{\langle t_{\mathrm{zero},n} \rangle c_{\mathrm{total}}(\mathrm{IBS1}^*)} \quad (5b)$$

$$\text{with } \langle t_{\mathrm{zero},n} \rangle = \frac{\left(\sum_{i=1}^{i\mathrm{max}} t_{\mathrm{zero},i,n}\right)}{i_{\mathrm{max}}} \quad \text{and} \quad \langle t_{\mathrm{high},n} \rangle = \frac{\left(\sum_{j=1}^{j\mathrm{max}} t_{\mathrm{high},j,n}\right)}{j_{\mathrm{max}}} \quad (5c)$$

$\langle t_{\mathrm{zero},n} \rangle$ and $\langle t_{\mathrm{high},n} \rangle$ are the mean dwell-times averaged over i_{max} and j_{max} dwell times of a molecule n. Note that i_{max} and j_{max} vary among different molecules and that $|i_{\mathrm{max}} - j_{\mathrm{max}}| = 1$ or 0. Mean dwell times of a molecule n in the high or zero *FRET* state are represented in Fig. 4A.

Averaged K_{A} values from single molecule *FRET* traces were calculated from the sum of all dwell times of the total number of analyzed molecules n_{max}.

$$K_{\mathrm{A}} = \frac{1}{K_{\mathrm{D}}} \cong \frac{t_{\mathrm{high}}^{\mathrm{sum}}}{t_{\mathrm{zero}}^{\mathrm{sum}} c_{\mathrm{total}}(\mathrm{IBS1}^*)} \quad (6a)$$

$$\text{with} \quad t_{\text{zero}}^{\text{sum}} = \sum_{n=1}^{n_{\max}} \sum_i t_{\text{zero},i,n} \qquad \text{and} \quad t_{\text{high}}^{\text{sum}} = \sum_{n=1}^{n_{\max}} \sum_j t_{\text{high},j,n} \tag{6b}$$

The Gibbs Free Energy $\Delta G°$ of single molecules was then calculated from K_A according to

$$\Delta G_n^0 \;=\; k_B T ln K_{D,n} = \; -k_B T ln K_{A,n} \tag{7}$$

where k_B equals the Boltzmann constant and T the absolute temperature.

Kinetic rates. Cumulative probability distributions $P(t_{zero})$ and $P(t_{high})$ were built according a method described by Hellriegel *et al.* (23). P was always normalized to 1, t_{zero} and t_{high} refer to the dwell times of molecules in the undocked and the docked FRET state with $t_{zero} = t_{zero,i,n}$ and $t_{high} = t_{high,j,n}$ for all i, j and n recorded under equal buffer conditions. Complementary cumulative probability distributions C were determined according to:

$$C(t_{\text{zero}}) = 1 - P(t_{\text{zero}}) \tag{8a}$$

and

$$C(t_{\text{high}}) = 1 - P\left(t_{\text{high}}\right) \tag{8b}$$

Subsequently, these distributions were fitted to exponential decay functions (24-26):

$$C(t_{\text{zero}}) = \sum_{m=1}^{m_{\max}} a_{\text{zero},m} exp\left\{-\frac{t_{\text{zero}}}{\tau_{\text{zero},m}}\right\} \tag{9a}$$

$$C(t_{\text{high}}) = \sum_{m=1}^{m_{\max}} a_{\text{high},m} exp\left\{-\frac{t_{\text{high}}}{\tau_{\text{high},m}}\right\} \tag{9b}$$

where m_{max} denotes the total number of exponential decay functions required to satisfactorily describe the experimental data. $a_{zero,m}$ and $a_{high,m}$ refer to the corresponding amplitudes. The kinetic rate constants k_{dock} and k_{undock} were determined from the resulting time constants τ_{zero} and τ_{high}:

$$k_{\mathrm{undock},m} = \frac{1}{\tau_{\mathrm{high},m}} \tag{10a}$$

$$k_{\mathrm{dock},m} = \frac{1}{\tau_{\mathrm{zero},m}\, c_{\mathrm{total}}(\mathrm{IBS1}^*)} \tag{10b}$$

Affinity/dissociation constants in the absence of M^{2+} (Table S1) were then calculated according to

$$K_{\mathrm{A},m} = \frac{k_{\mathrm{dock},m}}{k_{\mathrm{undock},m}} = \frac{\tau_{\mathrm{high},m}}{\tau_{\mathrm{zero},m} c_{\mathrm{total}}(\mathrm{IBS1}^*)} = \frac{1}{K_{\mathrm{D},m}} \tag{10c}$$

Calculation of $K_{A,n}$ distributions. To predict the fraction of d3'EBS1* molecules in the undocked state $P(<0.375)$ at varying c(IBS1*), the heterogeneity of the binding constants was accounted for by introducing l_{total} subspecies with binding constants $K_{\mathrm{A},l}$ that occur in certain fractions f_l. These conditions are implemented in Eq. 11 by transposition and modification of Eq. 4:

$$\frac{p(FRET_{\mathrm{zero}})}{p(FRET_{\mathrm{zero}}) + p\left(FRET_{\mathrm{high}}\right)} = \frac{t_{\mathrm{zero}}}{t_{\mathrm{zero}} + t_{\mathrm{high}}} = \sum_{l}^{l_{\mathrm{total}}} \frac{f_l}{K_{\mathrm{A},l} c(\mathrm{IBS1}^*) + 1} \tag{11a}$$

with $\sum f_l = 1$. Please refer to the next section for a description of the approach employed to extract discrete $K_{\mathrm{A},l}$ from statistically broadened cumulative probability distributions $P(K_{\mathrm{A},n})$. It must be emphasized that the obtained values $K_{\mathrm{A},l}$ may not be regarded as discrete. Rather, they are average values over a more or less continuous distribution of molecules, where f_l refers to the fraction of molecules close to the value $K_{\mathrm{A},l}$ (27). The averaged undocked fractions of d3'EBS1* for several hundreds of molecules ($n_{\max} > 200$) were determined with $t_{\mathrm{high}} = t_{\mathrm{high}}^{\mathrm{sum}}$ and $t_{\mathrm{zero}} = t_{\mathrm{zero}}^{\mathrm{sum}}$ (see Eq. 6b). Eq. 11a holds true when (i) the d3'EBS1* immobilization does not interfere with IBS1* docking/undocking, (ii) the underlying mechanism can be quantitatively described by a standard bimolecular reaction, and (iii) c_{total}(IBS1*) >> c(d3'EBS1*). The docked fraction is calculated in an analogous manner:

$$\frac{p\left(FRET_{\mathrm{high}}\right)}{p(FRET_{\mathrm{zero}}) + p\left(FRET_{\mathrm{high}}\right)} = \frac{t_{\mathrm{high}}}{t_{\mathrm{zero}} + t_{\mathrm{high}}} = 1 - \sum_{l}^{l_{\mathrm{total}}} \frac{f_l}{K_{\mathrm{A},l} c_{\mathrm{total}}(\mathrm{IBS1}^*) + 1} \tag{11b}$$

Mathematical description of the width of the $K_{A,n}$ distribution. Through combination of Eqs. 5b and 5c, the $K_{\mathrm{A},n}$ value can be calculated for an individual d3'EBS1* molecule n:

$$K_{\mathrm{A},n} \cong \frac{\langle t_{\mathrm{high},n}\rangle}{\langle t_{\mathrm{zero},n}\rangle[IBS1*]} = \frac{\frac{\left(\sum_{j=1}^{j\max} t_{\mathrm{high},j,n}\right)}{j_{\max}}}{\frac{\left(\sum_{i=1}^{i\max} t_{\mathrm{zero},i,n}\right)}{i_{\max}} c(\mathrm{IBS1}^*)} \quad (12)$$

Statistical nature of the docking/undocking process. The dwell-times $t_{\mathrm{zero},n,i}$ and $t_{\mathrm{high},n,j}$ are exponentially distributed according to the Markovian nature of binding and folding processes (22, 25, 26). Therefore, histograms of $t_{1,n,i}$ and $t_{2,n,j}$ are typically fitted to exponential models (25, 26). In heterogeneous systems, the dwell-time histograms require more than one exponential fit functions to be approximated (28). As $K_{\mathrm{A},n}$ depends directly on the average dwell times $\langle t_{\mathrm{zero},n}\rangle$ and $\langle t_{\mathrm{high},n}\rangle$ in the undocked and docked state (see Eq. 12), the uncertainty of $K_{\mathrm{A},n}$ depends on $i_{\max}$ and $j_{\max}$ (29). Finite length of smFRET time traces is therefore expected to broaden the $K_{\mathrm{A},n}$ frequency distribution, even for a homogeneous system with a single K_{A} (29). A mathematical description of the width of $K_{\mathrm{A},n}$ distributions for a homogeneous system and its dependence on $i_{\max}$ and $j_{\max}$ is quantitatively modeled below.

Cumulative probability distributions $P(K_{\mathrm{A},n})$ are binning-free and make use of the same formalism as for the dwell time distributions $P(t_{\mathrm{zero/high}})$ (23). According to Eq. 12, $K_{\mathrm{A,n}}$ depends on three parameters: c(IBS1*) (constant), $\langle t_{\mathrm{zero},n}\rangle$ and $\langle t_{\mathrm{high},n}\rangle$, the latter of which display inherent statistical fluctuations. Given the assumption that the system is homogeneous and the principle of ergodicity applies (30), it is possible to determine the overall K_{A} by fitting the distribution $p(K_{\mathrm{A},n})$ or $P(K_{\mathrm{A},n})$ from a sufficiently high number individual molecules with an appropriate analytical function.

Case 1: $i_{\max} = j_{\max} = 1$. Here, the distribution of $p(K_{\mathrm{A},n})$ corresponds to the ratio distribution of two exponential distributions $p(<t_{\mathrm{high},j,n}>)$ and $p(<t_{\mathrm{zero},i,n}>)$ with the analytical solution:

$$p\left(K_{\mathrm{A},n}\right) = \frac{p(\langle t_{\mathrm{high},n}\rangle_{j=1})}{c(\mathrm{IBS1}^*)p\left(\langle t_{\mathrm{zero},n}\rangle_{i=1}\right)} = \frac{[exp]_{\tau_{\mathrm{high}}}}{c(\mathrm{IBS1}^*)[exp]_{\tau_{\mathrm{zero}}}} = A\frac{R}{(1+R\cdot K_{\mathrm{A},n})^2} \quad (13a)$$

In general, the time constants τ_{high} and τ_{zero} are the expected values of dwell times in state 1 and state 2, A is an amplitude to account for the number of events in an experimental (not normalized) frequency distribution and the true K_{A} can be derived by $K_{\mathrm{A}} = 1/R$. Please refer to Fig. S14A (top) for a visual representation of this case. Please note that $R \sim \tau_{\mathrm{zero}}/\tau_{\mathrm{high}}$.

Case 2: $i_{\max} = j_{\max} > 1$. Here, $p(<t_{\mathrm{high},j,n}>)$ and $p(<t_{\mathrm{zero},i,n}>)$ are no longer exponentially distributed, since

the exponentially distributed values are averaged over i_{max} or j_{max} number of dwell times. Again, $\langle t_{\mathrm{FRET},i_{\mathrm{max},n}} \rangle$ corresponds to the average time a molecule n dwells in a certain *FRET* state (Eq. 5c). Thus the distribution of $p(K_{A,n})$ is no longer the ratio of two exponential distributions, but the ratio distribution of two gamma distributions with the expected values τ_{high} and τ_{zero}:

$$p(K_{\mathrm{A},n}) = \frac{p(\langle t_{\mathrm{high},n} \rangle_{i\geq 1})}{c(\mathrm{IBS1}^*)p(\langle t_{\mathrm{zero},n} \rangle_{i\geq 1})} = \frac{[gamma]_{\tau_{\mathrm{high}}}}{c(\mathrm{IBS1}^*)[gamma]_{\tau_{\mathrm{zero}}}} \tag{13b}$$

Averaging monoexponentially distributed dwell times yields a probability distribution $p(\langle t_{\mathrm{zero},i_{\mathrm{max},n}} \rangle)$, which is analytically described by a gamma distribution (28, 31). In this context, it is defined as follows:

$$p_{\Gamma}(\langle t_{\mathrm{zero},i_{\mathrm{max},n}} \rangle) = A \, \frac{k^{i_{\mathrm{max}}} \langle t_{zero,i_{\mathrm{max},n}} \rangle^{i_{\mathrm{max}}-1}}{\Gamma(i_{\mathrm{max}})} e^{-k\langle\langle t_{\mathrm{zero},i_{\mathrm{max},n}} \rangle\rangle} \tag{13c}$$

where $k = 1/\tau_{zero}$, A is an amplitude, Γ is the gamma function, and i_{max} the number of dwell times used for averaging, which ultimately defines the width of the Gamma distribution. In order to quantitatively assess case 2, we computed dwell-time histograms $p(\langle t_{\mathrm{dwell},i_{\mathrm{max},n}} \rangle)$ from 10000 simulated smFRET time traces with $i_{max} = j_{max} = 1$, 3, 5, 10, 30 or 90 and fitted them to Eq. 13c. Fig. S14A clearly shows that Eqs. 13a and 13c describe the simulated distributions $p(\langle t_{\mathrm{zero},i_{\mathrm{max},n}} \rangle)$ very well. Please note that high values for i_{max} and j_{max} lead to considerable narrowing of the simulated distributions, as would be expected for *FRET* time trajectories with a high number of transitions (22). Simulations were performed in MATLAB (release 2013b, license of the University of Zurich) using the built-in function "random('exp',・ ・)".

The ratio distribution of two gamma distributions has been described by Coelho and Mexia:

$$\begin{aligned} p(K_{\mathrm{A},n}) &= \frac{[gamma]_{\tau_{\mathrm{high}}}}{c(\mathrm{IBS1}^*)[gamma]_{\tau_{\mathrm{zero}}}} = \frac{p_{\Gamma}(\langle t_{\mathrm{high},n,i_{\mathrm{max}}} \rangle)}{[IBS1*]p_{\Gamma}(\langle t_{\mathrm{zero},n,j_{\mathrm{max}}} \rangle)} \\ &= \frac{k^N}{B(N,N)} (1 + R{K_{\mathrm{A},n}}^{-2N}) {K_{\mathrm{A},n}}^{N-1} \end{aligned} \tag{14a}$$

with $N := i_{max} = j_{max}$, and $R = 1/K_A$. Note that $R \sim \tau_{zero}/\tau_{high} \sim k_{dock}/k_{undock}$. $B(N,N)$ is the so-called beta

function (32). To account for the variable number of events, an amplitude A was introduced, expanding Eq. 14a as follows:

$$p(K_{A,n}) = A\frac{{K_A}^{-N}}{B(N,N)}(1+\frac{K_{A,n}}{K_A})^{-2N}{K_{A,n}}^{N-1} \quad (14b)$$

Note that working with the distributions of log K_A, denoted p(log $K_{A,n}$), and hence substitution of K_A by $10^{\log K_A}$ as well as of $K_{A,n}$ by $10^{\log K_{A,n}}$, the factor of $10^{logK_{A,n}}\ln(10)$ needs to be multiplied to eq. (14b) yielding eq. (14c):

$$p(logK_{A,n}) = A\frac{(10^{logK_A})^{-N}}{B(N,N)}\left(1+\frac{10^{logK_{A,n}}}{10^{logK_A}}\right)^{-2N}(10^{logK_{A,n}})^{N-1}\cdot 10^{logK_{A,n}}\ln(10) \quad (14c)$$

Fig. S14B shows the distributions of n_{max} = 10000 computed $K_{A,n}$ values with i_{max} = j_{max} = 1, 3, 5, 10, 30 and 90 exponentially distributed dwell-times in the high and zero *FRET* state. Approximation of the simulated data using Eq. 14b results in an excellent fit. Simulations were performed in MATLAB (release 2010b, license of the University of Zurich) using the built-in function "random('exp',・・)".

It is preferable to plot such distributions in a cumulative manner, because the result is not dependent on the bin size, a method routinely used in diffusion analysis (23, 33). Fig. S14C shows a cumulative probability distribution $P(K_{A,n})$ of the simulated data from Fig. S14B normalized to 1. As fitting $P(K_{A,n})$ distributions to the integral over Eq. 14b is rather cumbersome, we prefer a numerical approximation.

Approximation of intermolecular heterogeneity. Logistic functions are well known and widely applied in many fields, for example to describe a bimolecular association (34, 35). Fig. S14C demonstrates that the cumulative probability distributions $P(K_{A,n})$ can be very well approximated using the logistic function as defined in Origin 9.0 (OriginLab Coorp., Northhampton, MA, USA):

$$P(K_{A,n}) = \frac{A_1 - A_2}{1+(K_{A,n}/K_A)^p} + A_2 \quad (15a)$$

Here, the parameter p determines the steepness of the transition in $P(K_{A,n})$, *i.e.* the width of $p(K_{A,n})$, as described above. A_1 and A_2 are the lower and upper boundaries of the sigmoid. The relation between

p and i_{max} (and j_{max}) is illustrated in Fig. S15. Normalization ($A_1 = 0$ and $A_2 = 1$) yields:

$$P^{\mathrm{norm}}(K_{\mathrm{A},n}) = \frac{1}{1 + (K_{\mathrm{A}}/K_{\mathrm{A},n})^p} = 1 - \frac{1}{1 + (K_{\mathrm{A},n}/K_{\mathrm{A}})^p} \tag{15b}$$

Substituting $K_{\mathrm{A,n}}$ with $10^{\log K_{\mathrm{A,n}}}$, Eq. 15b turns into:

$$\begin{aligned} P^{\mathrm{norm}}(\log K_{\mathrm{A},n}) &= 1 - \frac{1}{1 + \left(\frac{10^{\log K_{\mathrm{A},n}}}{10^{\log K_{\mathrm{A}}}}\right)^p} = 1 - \frac{1}{1 + \left(10^{\log K_{\mathrm{A},n} - \log K_A}\right)^p} \\ &= \frac{1 + \left(10^{\log K_{\mathrm{A},n} - \log K_{\mathrm{A}}}\right)^p - 1}{1 + \left(10^{\log K_{\mathrm{A},n} - \log K_{\mathrm{A}}}\right)^p} = \frac{\left(10^{\log K_{\mathrm{A},n} - \log K_{\mathrm{A}}}\right)^p}{1 + \left(10^{\log K_{\mathrm{A},n} - \log K_{\mathrm{A}}}\right)^p} \end{aligned} \tag{15c}$$

Substitution of -logK_{A} by pK_{A} yields:

$$P^{\mathrm{norm}}(\mathrm{p}K_{\mathrm{A},n}) = \frac{(10^{-pK_{\mathrm{A},n} + pK_{\mathrm{A}}})^p}{1 + (10^{-pK_{\mathrm{A},n} + pK_{\mathrm{A}}})^p} \tag{15d}$$

Please note that for $p = 1$ Eq. 15d is equivalent to Eq. 16b, which is well-known to describe a simple acid-base equilibrium:

$$\mathrm{A^-} + \mathrm{H^+} \rightleftharpoons \mathrm{AH} \tag{16a}$$

$$f = \frac{f_{\mathrm{A}} + f_{\mathrm{AH}}\, 10^{(pK_{\mathrm{AH}} - pH)}}{1 + 10^{(pK_{\mathrm{AH}} - pH)}} \tag{16b}$$

where f corresponds to the fraction of protonated HA (fully deprotonated: $f_{\mathrm{A}} = 0$, fully protonated: $f_{\mathrm{AH}} = 1$) in a normalized from, for example in chemical shift mapping using NMR (36). Eqs. 15d and 16b are equivalent with exception of the parameter p. In a normal acid-base equilibrium, the slope of the transition is not variable ($p = 1$), and does therefore not provide any information about the system. In turn, single-molecule FRET experiments have finite observation time, leading to cross-sample variability and p values greater than 1.

Eq. 15d describes a homogeneous system with one averaged K_{A} value. Description of a heterogeneous system is achieved by introducing an amplitude a_s and by describing $P^{\mathrm{norm}}(K_{\mathrm{A},n})$ as a linear combination of the total number s_{max} of components $K_{\mathrm{A},s}$:

$$P^{\mathrm{norm}}(K_{\mathrm{A},n}) = \sum_{s=1}^{s_{\max}} a_s \frac{1}{1+(\frac{K_{\mathrm{A},s}}{K_{\mathrm{A},n}})^p}; \sum_{s=1}^{s_{\max}} a_s = 1 \quad (17a)$$

$$P^{\mathrm{norm}}(logK_{\mathrm{A},n}) = \sum_{s=1}^{s_{\max}} a_s \frac{\left(10^{\log K_{\mathrm{A},n}-\log K_{\mathrm{A},s}}\right)^p}{1+\left(10^{\log K_{\mathrm{A},n}-\log K_{\mathrm{A},s}}\right)^p} \quad \text{with} \quad \sum_{s=1}^{s_{\max}} a_s = 1 \quad (17b)$$

Approximation of the experimental data with $P^{\mathrm{norm}}(K_{\mathrm{A},n})$ according to Eq. 17a requires the value of p to be known. p depends on the number of transitions between different *FRET* states ($i_{\max}$ and $j_{\max}$, Fig. S15), which are usually not constant between individual time traces (Fig. 1). In the experiments presented herein, $i_{\max}$ and $j_{\max}$ range between 2 and 7 for the majority of molecules with a median value of approximately 3.5.

The formalism described above serves as a tool to extract information about the number of molecules a_s populating $K_{\mathrm{A},s}$ values within a certain range in the case of a heterogeneous system. Such, the overall docked fractions at different molar ratios of d3'EBS1*/IBS1* can be computed. The experimental distributions $P^{\mathrm{norm}}(\log K_{\mathrm{A},n})$ were fit to Eq. 17b, yielding the binding constants $\log K_{\mathrm{A},s}$ shown in Tables S3 and S4.

Calculation of the association constants logK_A of Mg^{2+} to d3'EBS1* and d3'EBS1*/IBS1*. Mg^{2+}-induced chemical shift changes $\Delta\delta$ were determined by adding 0, 0.5, 1, 1.5, 2, 2.5, 3, 4, 5, 6, 6.5 and 7 mM $MgCl_2$ to d3'EBS1* or d3'EBS1*/IBS1* dissolved in D_2O, respectively. Upon each titration step, a [^{1}H,^{1}H]-NOESY spectrum (d3'EBS1*: 293 K, 10 mM KCl, 10 µM EDTA; d3'EBS1*/IBS1*: 298 K, 110 mM KCl, 10 µM EDTA) was recorded as described in (37).

The Δδ values corresponding to ribose H1' protons and base H5, H6, H8 and H2 protons were fitted to a 1:1 binding isotherm for each Mg^{2+} concentration:

$$\delta_{\mathrm{obs}} = \delta_{\mathrm{RNA}} + (\delta_{\mathrm{RNA\cdot M^{2+}}} - \delta_{\mathrm{RNA}}) \frac{[M^{2+}] + c(\mathrm{RNA}) + \frac{1}{K_{\mathrm{A}}} - \sqrt{\left([\mathrm{M^{2+}}] + c(\mathrm{RNA}) + \frac{1}{K_{\mathrm{A}}}\right)^2 - 4[\mathrm{M^{2+}}]c(\mathrm{RNA})}}{2c(\mathrm{RNA})} \quad (18)$$

where δ_{RNA} is the chemical shift value of the proton in the absence of divalent metal ions and $\delta_{RNA\text{-}M^{2+}}$ is the chemical shift of the proton in the RNA-metal complex (38). Poorly fitted titration curves were discarded and protons with similar K_A values were grouped according to the previously defined Mg^{2+}-binding sites (37):

d3'EBS1*:

Stem: A3H1', G4H1', G4H8, U5H1', U5H6, A25H8, C26H1', C26H6, U27H1', U27H6

Loop: A10H1', A10H2, A10H8, U11H1', U1H5, U11H6, U12H1', U12H6, G21H1', A20H1', A20H2, A20H8

d3'EBS1*/IBS1*:

Stem: A3H1', G4H1', G4H8, U5H6, A25H2, C26H1', C26H6, U27H6

Loop 1: G13H1', G13H8, G14H1', G14H8

Loop 2: A16H2, A16H8, C17H6, U18H6, G19H1', A20H1', G21H1', G21H8, C59H1', C59H5, C59H6, A60H2, A60H8, G61H1', G61H8, U62H6, G63H1', G63H8, U64H1'

The average association constants of each binding site were refined iteratively using the MATLAB script ISTAR v2.3 as described in (39).

SUPPLEMENTARY REFERENCES

1. Ditzler MA, Rueda D, Mo J, Håkansson K, & Walter NG (2008) A rugged free energy landscape separates multiple functional RNA folds throughout denaturation. *Nucleic Acids Res.* 36(22):7088-7099.
2. König SLB, Huppert JL, Sigel RKO, & Evans AC (2013) Distance-dependent duplex DNA destabilisation proximal to G-quadruplex/i-motif sequences. *Nucleic Acids Res.* 41:7453-7461.
3. Mergny JL & Lacroix L (2003) Analysis of thermal melting curves. *Oligonucleotides* 13:515-537.
4. Blanco M & Walter NG (2010) Analysis of complex single-molecule FRET time trajectories. *Method. Enzymol.* 475:153-178.
5. Lakowicz JR (2006) *Principles of fluorescence spectroscopy* (Springer Science+Business Media, LCC, New York, NY, USA) 3 Ed.
6. Zhao R & Rueda D (2009) RNA folding dynamics by single-molecule fluorescence resonance energy transfer. *Methods* 49:112-117.
7. Cardo L, Karunatilaka KS, Rueda D, & Sigel RKO (2012) Single molecule FRET characterization of large ribozyme folding. *Methods Mol. Biol.* 848:227-251.
8. Ha T (2001) Single-molecule fluorescence resonance energy transfer. *Methods* 25:78-86.
9. Rasnik I, McKinney SA, & Ha T (2006) Nonblinking and long-lasting single-molecule fluorescence imaging. *Nat. Methods* 3(11):891-893.
10. Holden SJ*, et al.* (2010) Defining the limits of single-molecule FRET resolution in TIRF microscopy. *Biophys. J.* 99(9):3102-3111.
11. Lee S, Lee J, & Hohng S (2010) Single-molecule three-color FRET with both negligible spectral overlap and long observation time. *PLoS ONE* 5(8):e12270.
12. Chung S-H & Kennedy RA (1991) Forward-backward non-linear filtering technique for extracting small biological signals from noise. *J. Neurosci. Meth.* 40(1):71-86.
13. Haran G (2004) Noise reduction in single-molecule fluorescence trajectories of folding proteins. *Chem. Phys.* 307(2-3):137-145.
14. Ha T*, et al.* (1996) Probing the interaction between two single molecules: fluorescence resonance energy transfer between a single donor and a single acceptor. *Proc. Natl. Acad. Sci. USA* 93(13):6264-6268.
15. Wood S, Ferré-D'Amaré A, & Rueda D (2012) Allosteric interactions preorganize the c-di-GMP riboswitch and accelerate ligand binding. *ACS Chem. Biol.* 7(5):920-927.
16. König SLB*, et al.* (2013) BOBA FRET: Bootstrap-based analysis of single-molecule FRET data. *PloS ONE* 8(12):e84157.
17. Kapanidis AN*, et al.* (2004) Fluorescence-aided molecule sorting: analysis of structure and interactions by alternating-laser excitation of single molecules. *Proc. Natl. Acad. Sci. USA* 101(24):8936-8941.
18. König SLB, Liyanage P, Sigel RKO, & Rueda D (2013) Helicase-mediated changes in RNA structure at the single-molecule level. *RNA Biol.* 10:132-147.
19. Sabanayagam CR, Eid JS, & Meller A (2005) Long time scale blinking kinetics of cyanine fluorophores conjugated to DNA and its effect on Förster resonance energy transfer. *J. Chem. Phys.* 123(22):224708.
20. Cisse I, Okumus B, Joo C, & Ha T (2007) Fueling protein–DNA interactions inside porous nanocontainers. *Proc. Natl. Acad. Sci. USA* 104:12646-12650.
21. Aitken CE, Marshall RA, & Puglisi JD (2008) An oxygen scavenging system for improvement of dye stability in single-molecule fluorescence experiments. *Biophys. J.* 94(5):1826-1835.
22. Greenfield M, Pavlichin DS, Mabuchi H, & Herschlag D (2012) Single molecule analysis research tool (SMART): an integrated approach for analyzing single molecule data. *PloS ONE* 7(2):e30024.
23. Hellriegel C*, et al.* (2004) Diffusion of single streptocyanine molecules in the nanoporous network of sol-gel glasses. *J. Phys. Chem. B* 108:14699-14709.
24. Steiner M, Karunatilaka KS, Sigel RKO, & Rueda D (2008) Single-molecule studies of group II intron ribozymes. *Proc. Natl. Acad. Sci. USA* 105(37):13853-13858.
25. Zhuang X*, et al.* (2000) A single-molecule study of RNA catalysis and folding. *Science* 288(5473):2048-2051.
26. Zhuang X*, et al.* (2002) Correlating structural dynamics and function in single ribozyme molecules. *Science* 296(5572):1473-1476.

27. Hyeon C, Lee J, Yoon J, Hohng S, & Thirumalai D (2012) Hidden complexity in the isomerization dynamics of Holliday junctions. *Nat. Chem.* 4(11):907-914.
28. Flomenbom O*, et al.* (2005) Stretched exponential decay and correlations in the catalytic activity of fluctuating single lipase molecules. *Proc. Natl. Acad. Sci. USA* 102(7):2368-2372.
29. Solomatin SV, Greenfield M, Chu S, & Herschlag D (2010) Multiple native states reveal persistent ruggedness of an RNA folding landscape. *Nature* 463:681-684.
30. Walter NG, Huang C-Y, Manzo AJ, & Sobhy MA (2008) Do-it-yourself guide: how to use the modern single-molecule toolkit. *Nat. Methods* 5(6):475-489.
31. Floyd DL, Harrison SC, & van Oijen AM (2010) Analysis of kinetic intermediates in single-particle dwell-time distributions. *Biophys. J.* 99:360-366.
32. Coelho CA & Mexia JT (2007) On the distribution of the product and ratio of independent generalized gamma-ratio random variables. *Sankhya Ser. A* 69:221-255.
33. Krause S, Kowerko D, Börner R, Hübner CG, & von Borczyskowski C (2011) Spectral diffusion of single molecules in a hierarchical energy landscape. *ChemPhysChem* 12:303-312.
34. Britton NF (2003) Single species population dynamics. *Essential mathematical biology*, ed Britton NF (Springer, Berlin), pp 1-40.
35. Reed LJ & Berkson J (1929) The application of the logistic function to experimental data. *J. Phys. Chem.* 33(5):760-779.
36. Mitchell PR (1979) Hydrophobic interactions in ternary Zinc(II) and Copper(II) complexes containing 1,10-phenanthroline or 2,2'-bipyridyl and an alkane carboxylate or sulphonate. *Dalton Trans.*:771-776.
37. Kruschel D, Skilandat M, & Sigel RKO (2014) NMR structure of the 5'-splice site in the group IIB intron Sc.ai5γ – conformational requirements for positioning of the exon-intron junction. *RNA* 20:295-307.
38. Sigel RKO, Vaidya A, & Pyle AM (2000) Metal ion binding sites in a group II intron core. *Nat. Struct. Biol.* 7(12):1111-1116.
39. Erat MC & Sigel RKO (2007) Determination of the intrinsic affinities of multiple site-specific Mg(2+) ions coordinated to domain 6 of a group II intron ribozyme. *Inorg. Chem.* 46(26):11224-11234.
40. Mortier KA, Zhang GF, Van Peteghem CH, & Lambert WE (2004) Adduct formation in quantitative bioanalysis: effect of ionization conditions on paclitaxel. *J. Am. Soc. Mass Spectrom.* 15:585-592.
41. McKinney SA, Joo C, & Ha T (2006) Analysis of single-molecule FRET trajectories using hidden Markov modeling. *Biophys. J.* 91(5):1941-1951.
42. Cordes T*, et al.* (2010) Sensing DNA opening in transcription using quenchable Förster resonance energy transfer. *Biochemistry* 49:9171-9180.

SUPPLEMENTARY FIGURES

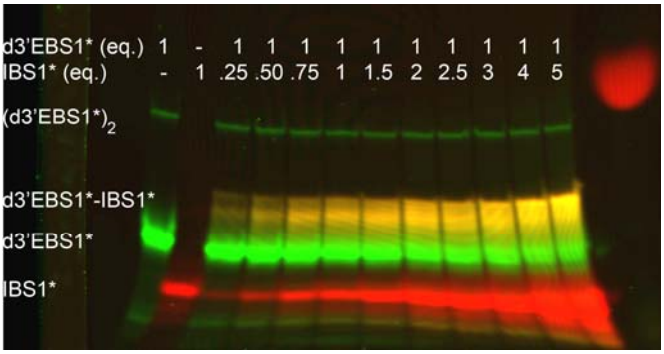

Fig. S1. d3'EBS1*/IBS1* affinity in the presence of Mg^{2+} and increasing IBS1* concentration as assessed with native gel electrophoresis (representative data; overlay). Four conformational species are observed and assigned as follows: $(d3'EBS1*)_2$ (upper green band), d3'EBS1*/IBS1* (yellow band), undocked d3'EBS1* (lower green band) and free IBS1* (red band). Migration was performed at 5 mM MOPS, 2 mM NaOH, 50 µM $MgCl_2$, pH 6.90.

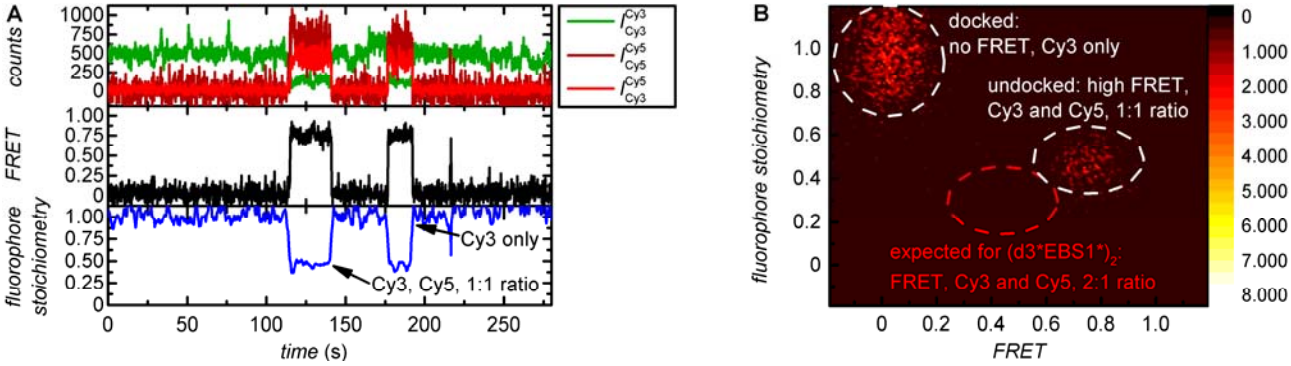

Fig. S2. smFRET control experiments I. **(A)** Top: ALEX yields three photon counts over time. Middle: *Apparent FRET* over time calculated according to Eq. 1. Bottom: f*luorophore stoichiometry* as determined according to Eq. 2 varies between 1 (undocked state), and 0.5 (docked state). Trace smoothed with sliding average over 10 data points. **(B)** 2D plot built from the data shown in (A). As expected from the experimental design, two populations are observed (28). IBS1* docked onto d3'EBS1* dimers (red area) or intermediate FRET efficiencies are not observed. The color code represents the number of counts. Imaging conditions: 50 mM MOPS, 100 mM KCl, 25 nM IBS1*, 1 % (w/V) D-Glucose, 1x OSS, 1 mM Trolox, pH 6.90.

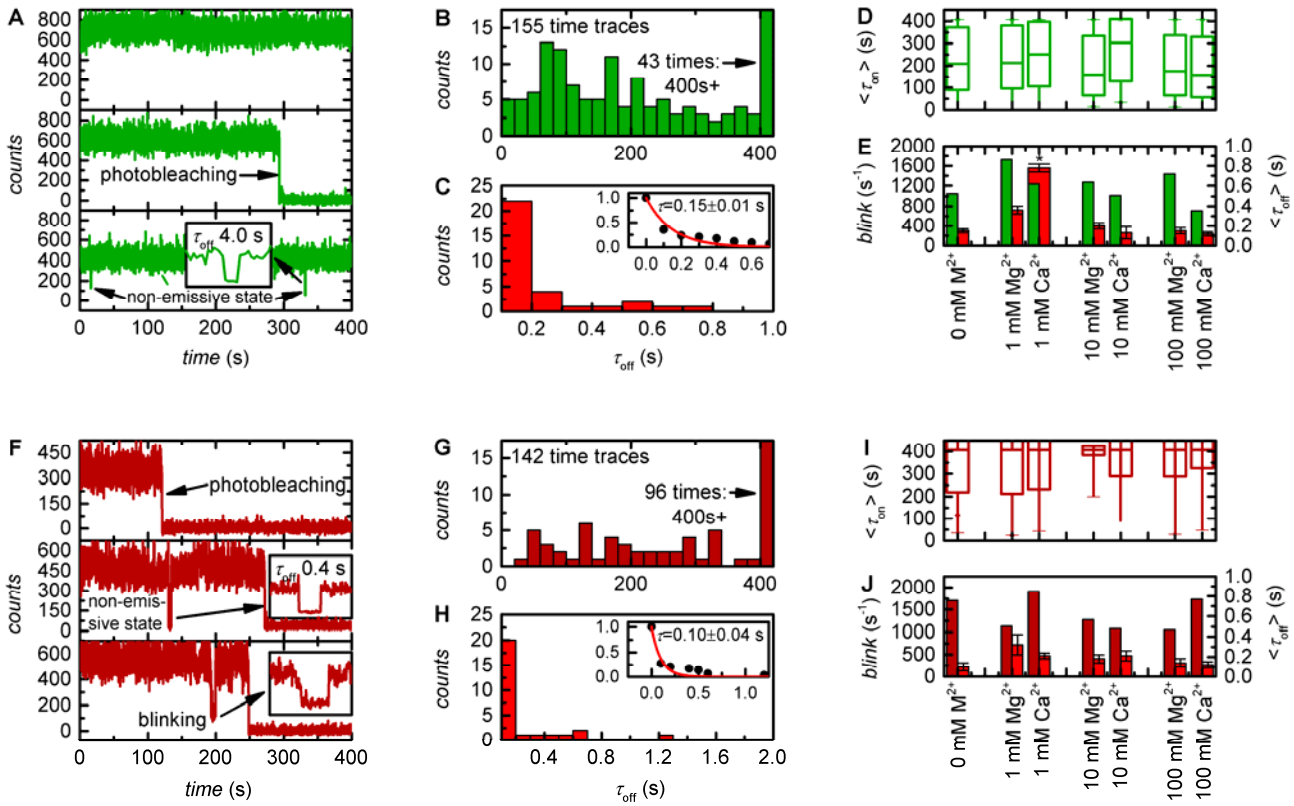

Fig. S3. smFRET control experiments II. **(A)** Representative *Cy3 emission* time trajectories show stable emission (top), photobleaching (middle), and blinking (bottom). **(B)** Time until Cy3 photobleaching (τ_{on}), representative data recorded at 0 mM M^{2+}. The histogram does not display a clearly defined statistical distribution, which may be due to a slow decay and/or the fact that dissociation of surface-immobilized RNA further complicates the kinetics. **(C)** Quantification of Cy3 blinking (τ_{off}), representative data recorded at 0 mM M^{2+}. The histogram data are very well described by a single-exponential decay model (red curve, inset). **(D)** Box plot of M^{2+}-dependent duration of stable Cy3 emission until photobleaching (line: median; box: upper/lower quartile; whiskers: minimum/maximum). Dwell times cover almost the full range of the observation time with a median centered around 200 s, demonstrating that the divalent metal ions assessed herein do not have a significant influence on Cy3 photostability. **(E)** M^{2+}-dependent Cy3 blink frequency and average duration of the dark state. The average time spent in the dark state $<\tau_{off}>$ is close to the time resolution in all cases and does not appear to be influenced by the presence of Mg^{2+} or Ca^{2+}. In turn, blinking becomes more frequent at high M^{2+} concentrations. **(F)** Representative *Cy5 emission* time trajectories unveil multistep blinking (middle, bottom). **(G)** Time until Cy5 photobleaching τ_{on}, representative data recorded at 0 mM M^{2+}. No underlying statistical distribution could be identified. **(H)** Quantification of Cy5 blinking τ_{off}, representative data recorded at 0 mM M^{2+}. The histogram data are in good agreement with a single-exponential decay model (red curve, inset). **(I)** Box plot of M^{2+}-dependent duration of stable Cy5 emission until photobleaching. Dwell times cover almost the full range, but the median reaches 400 s in all cases. **(J)** M^{2+}-dependent Cy5 blink frequency and average duration of the dark state. The average time spent in the dark state $<\tau_{off}>$ is close to the time resolution in all cases and is not influenced by Mg^{2+} or Ca^{2+}. The frequency at which blinking occurs does not appear to be cation-dependent, either. All errors correspond to the standard deviation 2σ as determined from single-exponential fits.

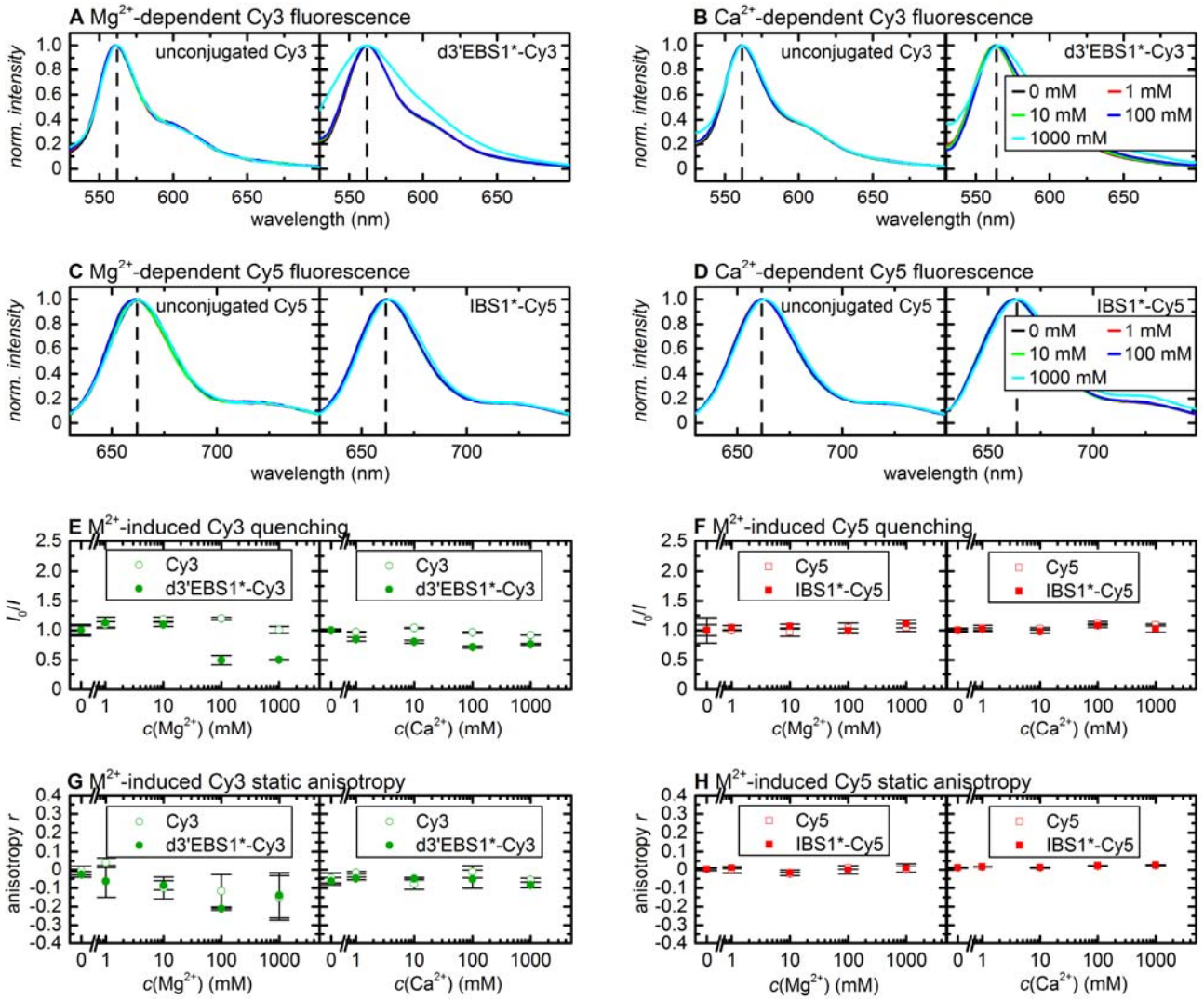

Fig. S4. Bulk fluorescence control experiments. **(A-D)** Mg^{2+}- and Ca^{2+}-dependent fluorescence spectra of Cy3-NHS ester, d3'EBS1*-Cy3, Cy5-NHS ester, and IBS1*-Cy5. Conjugation of the dye to RNA and the presence of divalent metal ion leaves the fluorescence spectra largely unaltered. Minor spectral broadening is observed for d3'EBS1*-Cy3 at 1000mM Mg^{2+}. **(E-F)** Stern-Volmer plots of Cy3 and Cy5 fluorescence as determined by fixed wavelength scans at $\lambda_{exc/em}$ = 530/560 nm and $\lambda_{exc/em}$ = 600/660 nm. While bioconjugation has a negligible effect, high divalent metal ion concentrations appear to quench Cy3 fluorescence. **(G-H)** Cation-dependent static anisotropy of Cy3 and Cy5 as determined by fixed wavelength scans at $\lambda_{exc/em}$ = 530/560 nm and $\lambda_{exc/em}$ = 600/660 nm. Differences were consistently within the accuracy of the method and suggest that fluorophore rotation is not significantly hindered by attaching the dye to RNA and/or the presence of divalent metal ions. Error bars correspond to the standard deviation 1σ.

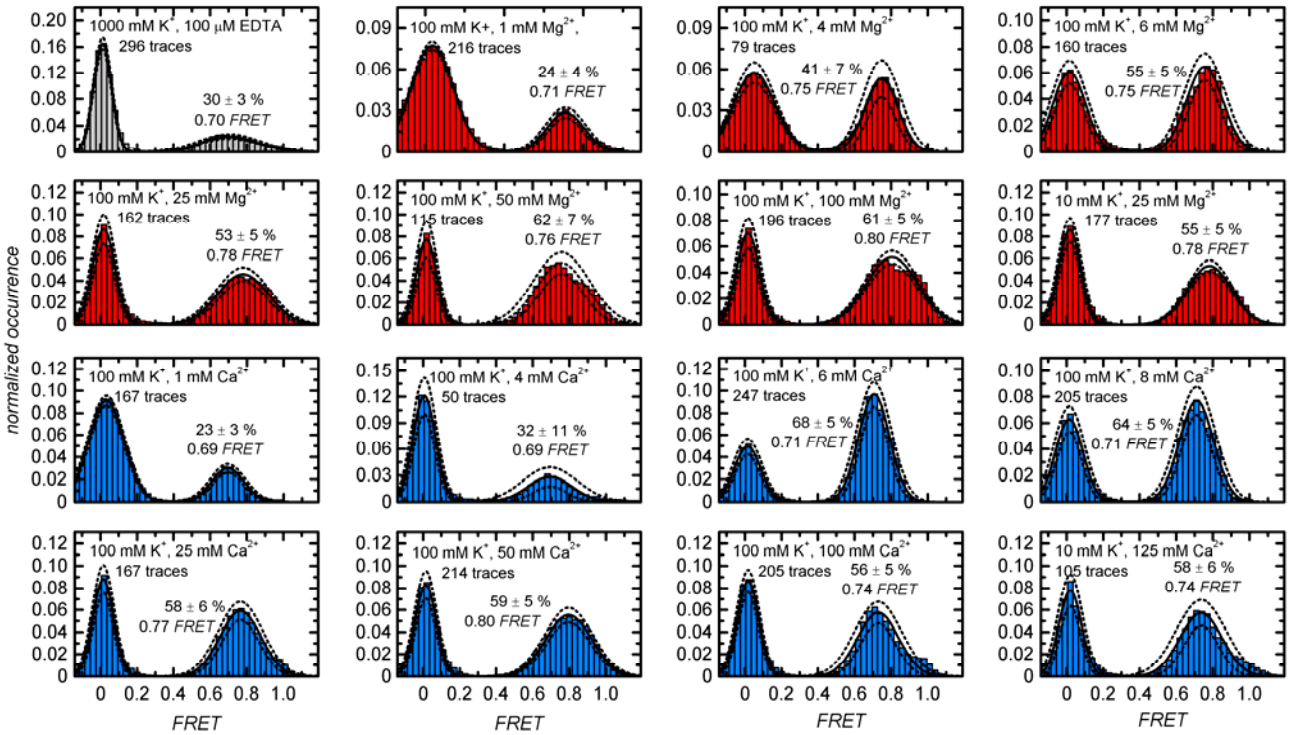

Fig. S5. Normalized cumulated histograms built from smFRET time traces recorded in different imaging buffers. The zero *FRET* distribution corresponds to undocked d3'EBS1*, while the high *FRET* peak corresponds to an IBS1* molecule docked onto d3'EBS1*. Values for *docked fractions*, the *center* values of the high *FRET* distribution, as well as the corresponding standard deviations 2σ were determined by bootstrapping and regression using BOBA FRET (16). Imaging conditions: 50 mM MOPS, 100 or 1000 mM KCl, 25 nM IBS1*, 1 % (w/V) D-Glucose, 1x OSS, 1 mM Trolox, pH 6.90, further additives as indicated.

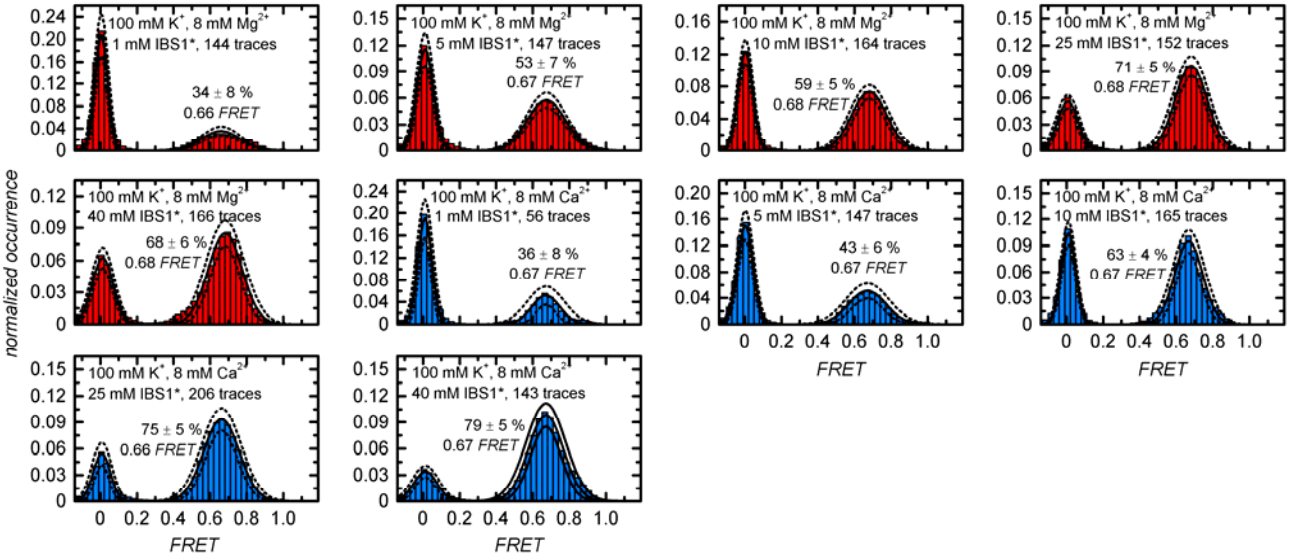

Fig. S6. Normalized cumulated histograms built from smFRET time traces recorded at constant M^{2+} concentration and increasing IBS1* concentration. Increasing IBS1* concentration favors the occurrence of the d3'EBS1*/IBS1* complex, *i.e.* the high *FRET* state. Values for *docked fractions*, the *center* values of the high *FRET* distribution, as well as the corresponding standard deviations 2σ were determined by bootstrapping and regression using BOBA FRET (16). Imaging conditions: 50 mM MOPS, 100 mM KCl, 8 mM $MgCl_2$, 1 % (w/V) D-Glucose, 1x OSS, 1 mM Trolox, pH 6.90, IBS1* as indicated.

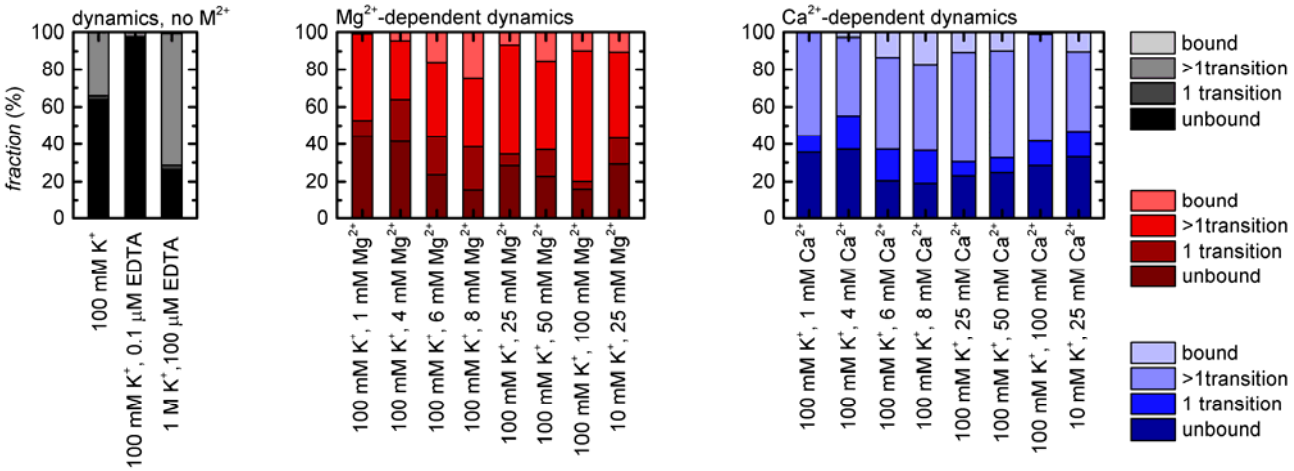

Fig. S7. Classification of time traces recorded at different ionic conditions. Time traces were classified as type I (>1 transition), type II (1 transition), type IIIa (static undocked), and type IIIb (static docked). For further details, please refer to the Supplementary Methods.

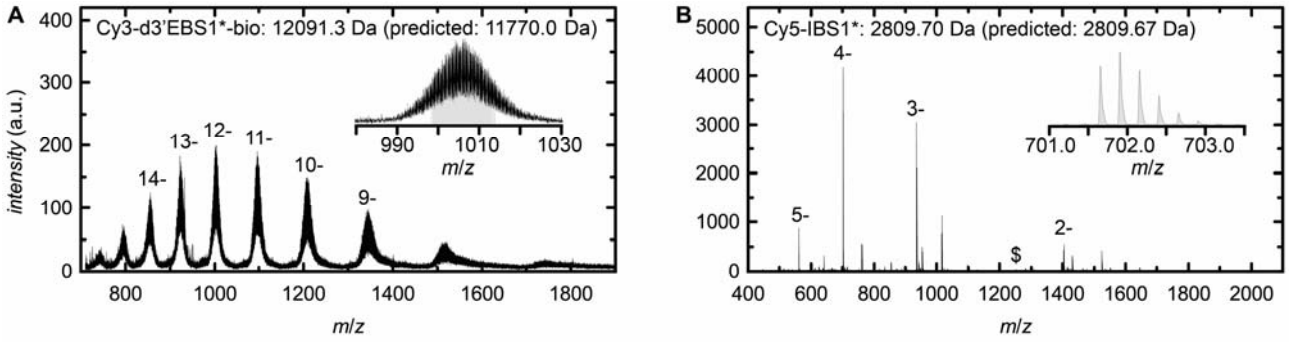

Fig. S8. Negative mode ESI mass spectra of **(A)** Cy3- and biotin-labeled d3'EBS1* and **(B)** Cy5-labeled IBS1*. Peak were generated from molecular ions at different charge states, as well as additional peaks with low abundance. The insets depict the 12- charge state of Cy3-d3'EBS1*-biotin and the 4- charge state of Cy5-IBS1*, respectively. The difference between the measured and the predicted mass of d3'EBS1* is most likely due to a mixed K^+/Na^+ adduct (M([d3'EBS1•K•12Na]) = 12097.8 g mol^{-1}), which is not unusual for long nucleic acids (40). The minor peak $ results from a loss of a cytidine monophosphate at the 3'-end of IBS1*.

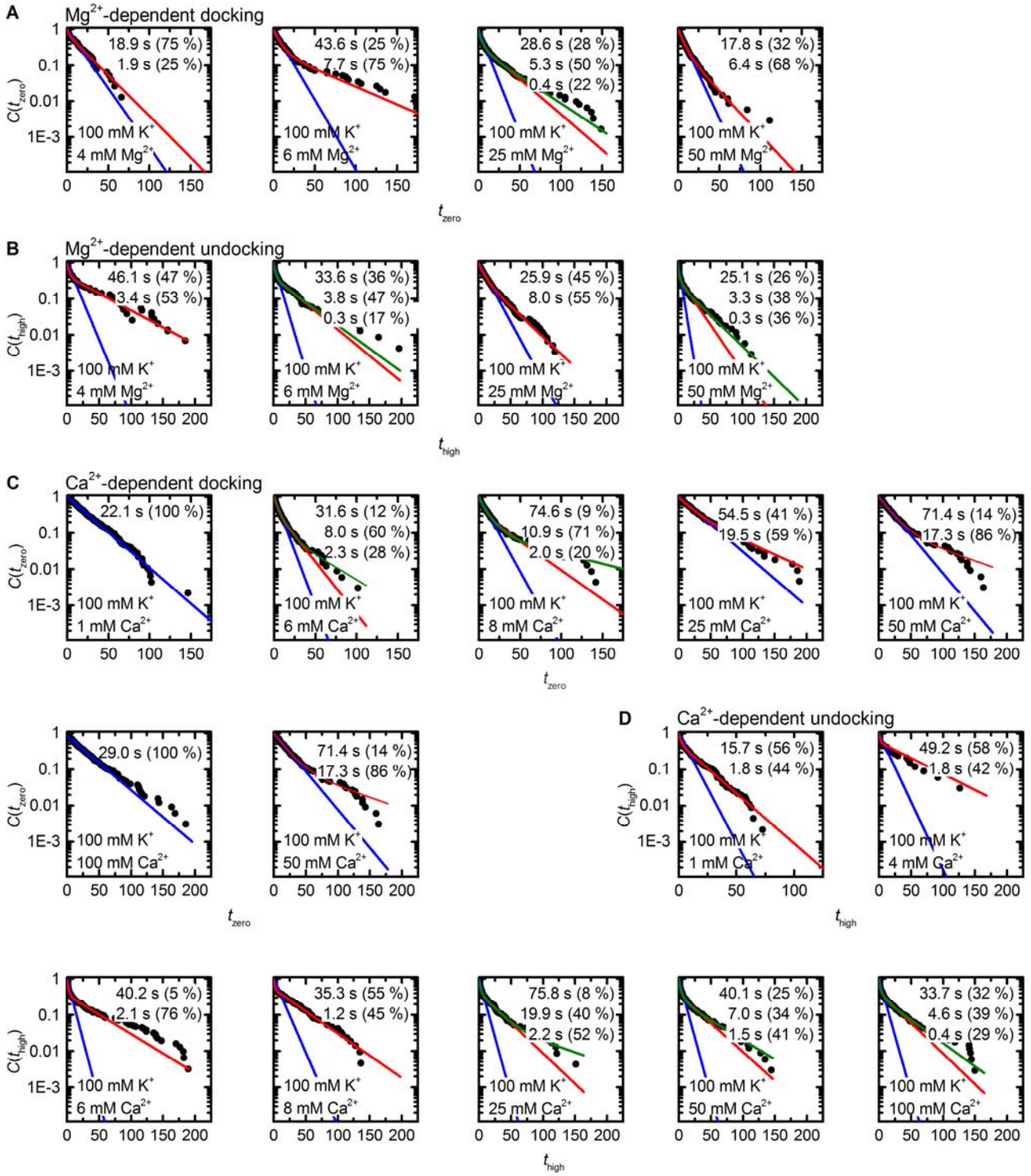

Fig. S9. Cumulative probability distributions of dwell times showing the decay of the zero *FRET* state $C(t_{zero})$ (see Eq. 8a), and the decay of the high *FRET* state $C(t_{high})$ (see Eq. 8b) in the presence of Mg^{2+} or Ca^{2+}. Blue: monoexponential decay, red: biexponential decay, green: triexponential decay.

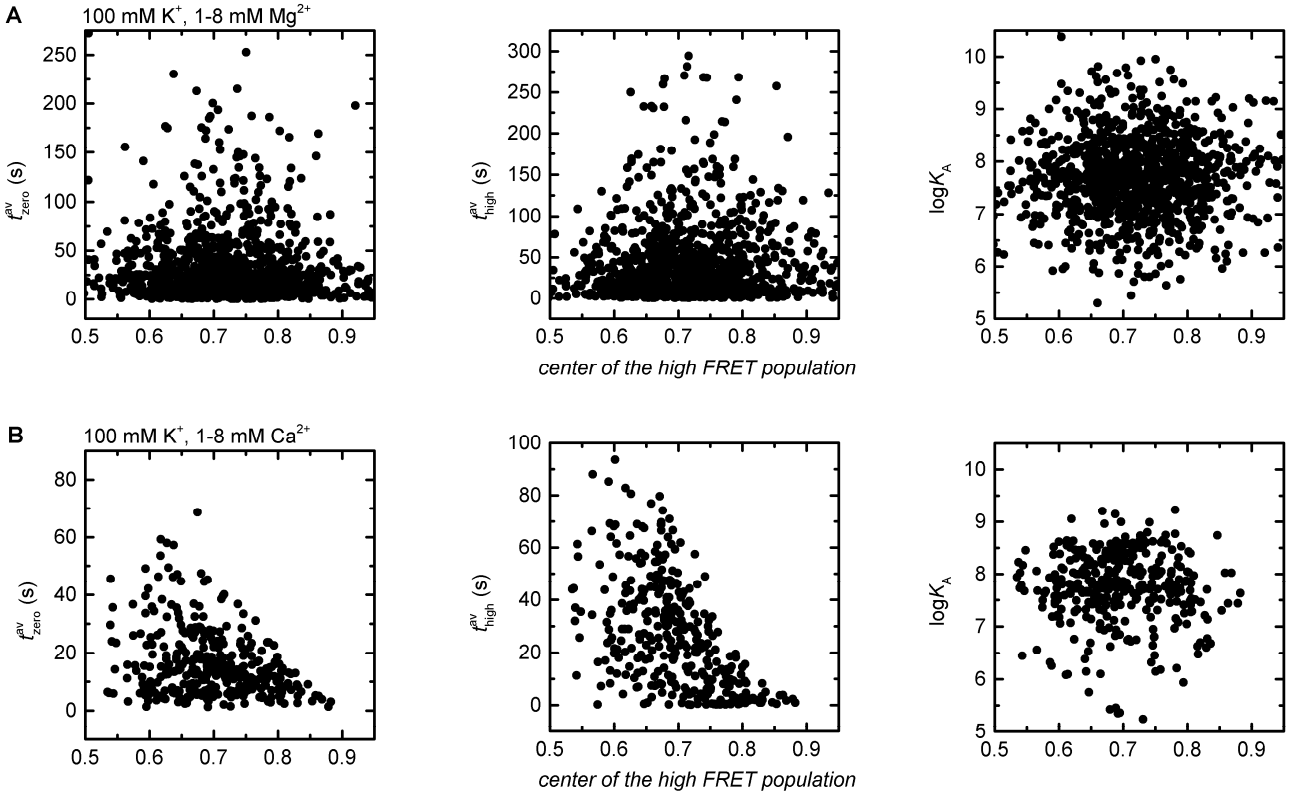

Fig. S10. Correlation of thermodynamic and kinetic heterogeneity of smFRET time traces recorded at 1-8 mM M^{2+}. Plotting the average dwell time in the zero *FRET* state (left), the average dwell time in the high *FRET* state (middle), and the average logK_A values of single molecules (right) against the center of the high *FRET* distribution does not reveal any clusters. Different high *FRET* values are therefore likely to be due to heterogeneous broadening (41).

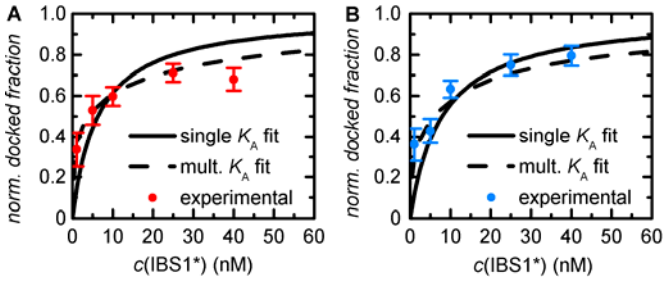

Fig. S11. IBS1*-dependent average docked fraction as determined from >200 smFRET time traces recorded at **(A)** 8 mM Mg^{2+} and **(B)** 8 mM Ca^{2+} (type IIIa molecules were omitted). Solid lines correspond to fits using Eq. 11b (l_{total} = 1, 1 logK_A value). Dashed lines correspond to fits using Eq. 11b (l_{total} = 4, 3 dynamic subpopulations with distinct logK_A values). Amplitudes (a_1, a_2, and a_3) and the corresponding logK_A values describing dynamic time traces were taken from Table S4, while static docked molecules (type IIIb) were approximated with log$K_{A,4}$ = 10. The sum of fractions f_1,...,f_4 was normalized to 1. Error bars correspond to $2\sigma_{bootstrap}$. The sum of the squared residuals for single versus multiple logK_A fits are 0.089 vs. 0.010 for Mg^{2+}, and 0.071 vs. 0.013 for Ca^{2+}, respectively. This clearly demonstrates that multiple logK_A fits describe the experimental data better than the single logK_A fits.

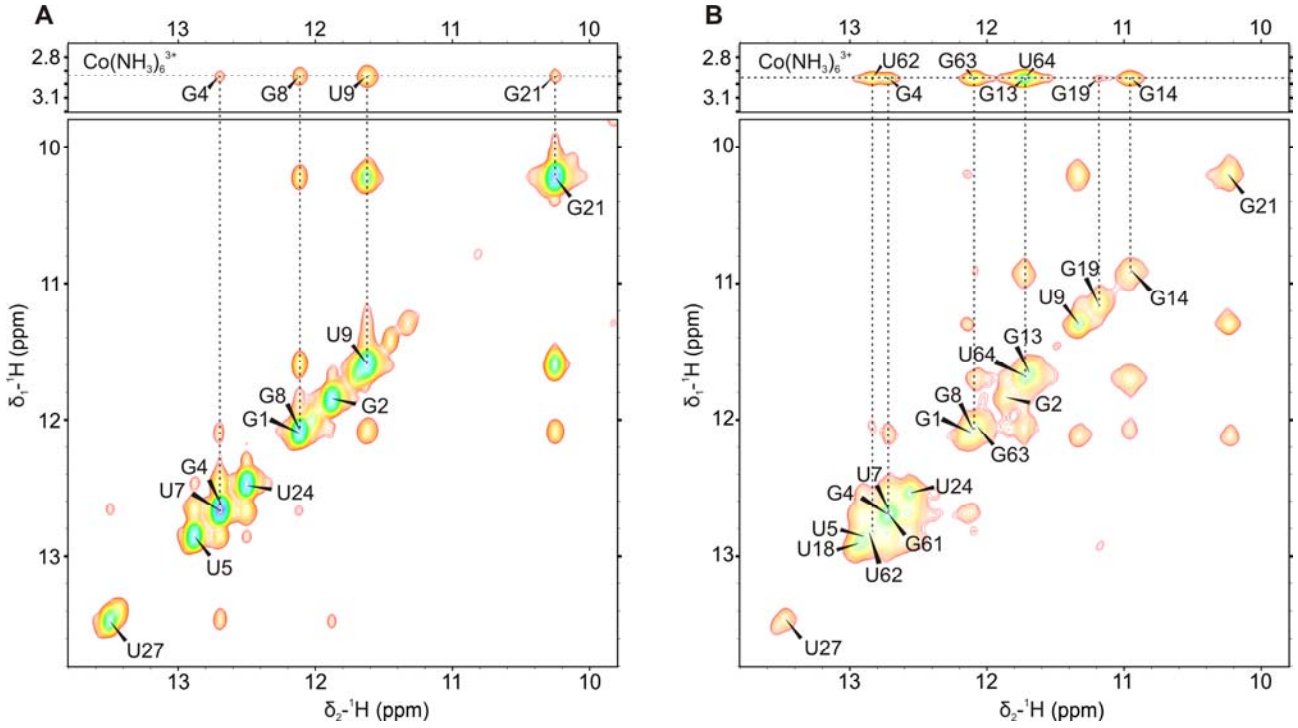

Fig. S12. Cobalt(III)hexammine binding to **(A)** d3'EBS1* and **(B)** d3'EBS1*/IBS1* as observed by NOE cross peaks in a [^{1}H,^{1}H]-NOESY between the ammine protons and the imino protons of the uracil and guanine nucleobases. Cobalt(III)hexammine binds in close proximity to the U9-G21 wobble pair in d3'EBS1*. In d3'EBS1*, this base pair seems not to bind cobalt(III)hexammine, but instead NOEs to nucleobases at/near the 5'-end of EBS1* (G13, G14 and U64) are observed. Spectra were recorded in 90 % H_2O/10 % D_2O at 278 K in 10 µM EDTA and 10 mM KCl, 2.5 mM $[Co(NH_3)_6]^{3+}$ (d3'EBS1*) and 110 mM KCl, 1.5 mM $[Co(NH_3)_6]^{3+}$ (d3'EBS1*/IBS1*). The RNA concentration was consistently set to 0.55 mM.

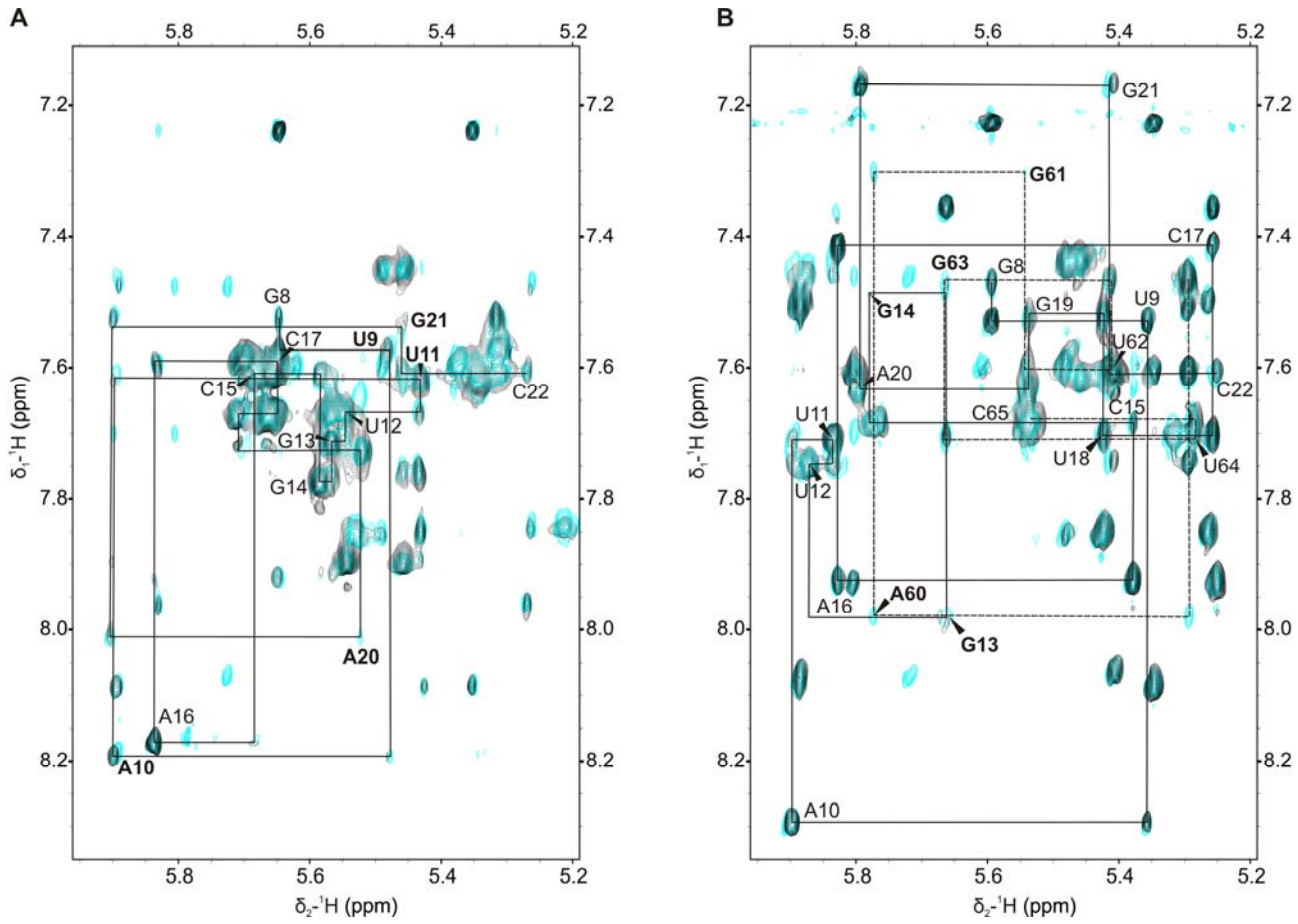

Fig. S13. Mn^{2+} binding to **(A)** d3'EBS1* and **(B)** d3'EBS1*/IBS1* as observed by paramagnetic line broadening in [^{1}H,^{1}H]-NOESY spectra of the non-exchangeable protons. Shown is a superposition of the spectra recorded in the absence of Mn^{2+} (cyan) or presence of 150 µM Mn^{2+} (black; d3'EBS1*) or 270 µM Mn^{2+} (black; d3'EBS1*/IBS1*) respectively. Cross peaks that have been broadened to base line at the given concentration of Mn^{2+} appear in cyan only. The sequential connectivities between H1' and H6/H8 protons of residues G8 and C22 are indicated as solid lines. Dashed lines visualize connectivities between residues C59-C65 of IBS1*. Residues mainly affected by Mn^{2+} are highlighted using bold face type. In the loop of d3'EBS1*, cross peaks between U9, A10 and U11 as well as cross peaks of A20 and G21 are most affected by broadening. In turn, cross peaks of G13, G14, A60 and G63 are the most affected peaks of the loop region within d3'EBS1*/IBS1*. Spectra were recorded in 100 % D_2O (d3'EBS1*: 0.54 mM RNA, 10 mM KCl, 10 µM EDTA, 293 K; d3'EBS1*/IBS1*: 0.6 mM RNA, 110 mM KCl, 10 µM EDTA, 298 K).

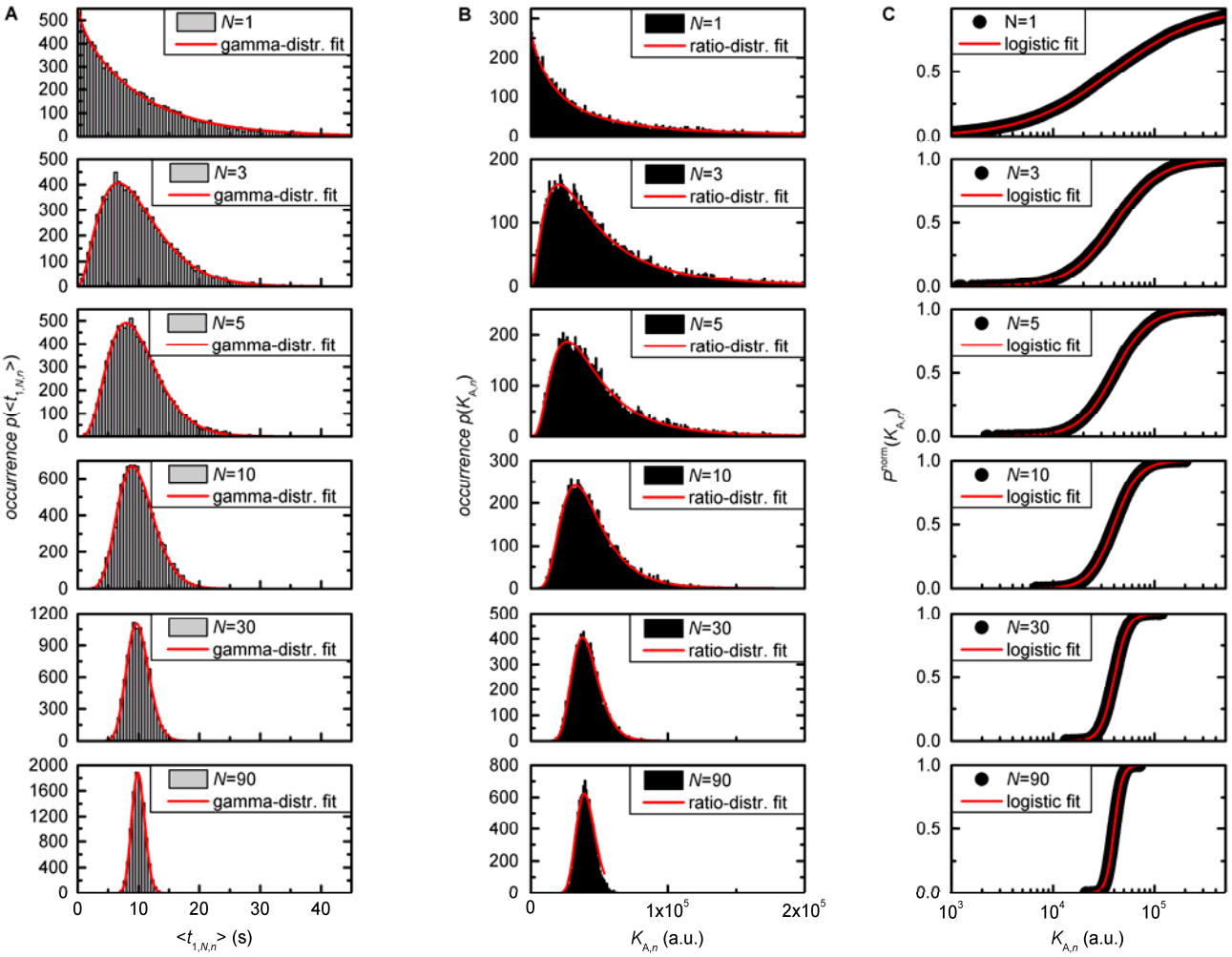

Fig. S14. Simulations of dwell-time and K_A distributions. **(A)** Dwell time histograms built from 10000 simulated single-molecule FRET time traces with $N := i_{max} = j_{max} = 1, 3, 5, 10, 30$, and 90 exponentially distributed dwell times. The red curves correspond to a gamma distribution fit using Eq. 13c. **(B)** $K_{A,n}$ histograms created from 10000 simulated single-molecule *FRET* time traces with the average time spent in the docked state $\tau_{high} = 10$ s and in the undocked state $\tau_{zero} = 10$ s. To calculate $K_{A,n}$ according to Eq. 5b, $c = 2.5 \times 10^{-8}$ M (which is equivalent to the IBS1* concentration in our experiments) and $N := i_{max} = j_{max} = 1, 3, 5, 10, 30$, or 90 exponentially distributed dwell times to determine $\langle t_{zero,n} \rangle$ and $\langle t_{high,n} \rangle$. The red curves correspond to a beta distribution fit according to Eq. 14b. **(C)** Cumulative probability distribution of the data shown in (B) fitted to Eq. 15b.

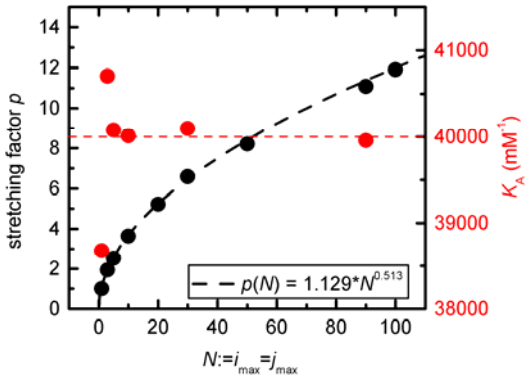

Fig. S15. The relation between shape parameter p and the number of dwell-times $N := i_{max} = j_{max}$ derived by fitting Eq. 13b to the graphs shown in Fig. S14C. When K_A is set to 4 x 10^7 M^{-1}, the simulations reveal that the smaller the number of dwell times during acquisition, the larger the deviation from K_A. For further details, please refer to the section "statistical nature of the docking/undocking processes" in the Supplementary Methods.

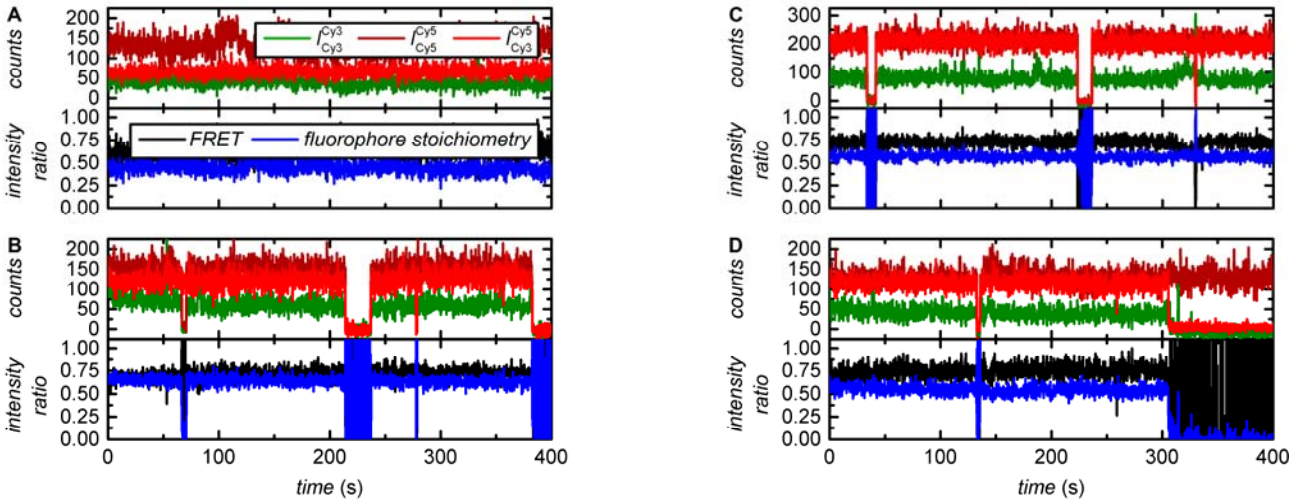

Fig. S16. Representative *fluorescence* and *intensity ratio* trajectories of co-encapsulated RNA molecules (Eqs. 1 and 2) (20). At 50 mM Mg^{2+}, single d3'EBS1*/IBS1* pairs predominantly populate the docked state and rarely undergo excursions to the undocked state. Visual inspection does not suggest any molecule-to-molecule heterogeneity. Stable emission profiles were observed in some cases **(A)**, though, the majority of time traces display donor-acceptor co-blinking **(B-D)**. Co-blinking is likely to be due to contact-induced quenching induced by close proximity of the dyes (42). Imaging conditions: 50 mM MOPS, 100 mM KCl, 50 mM $MgCl_2$, 1 % (w/V) D-Glucose, 1x OSS, 1 mM Trolox, pH 6.90.

SUPPLEMENTARY TABLES

Table S1. Thermodynamic parameters of the d3'EBS1*/IBS1* interaction in the presence of divalent metal ions as determined by UV thermal melting and smFRET. Errors correspond to the standard deviation (1σ).

Imaging buffer*	ΔG° (UV) (kJ mol^{-1})	ΔG° (smFRET) (kJ mol^{-1})	logK_A (smFRET)
no additives	-36.37 ± 0.33	-36.37 ± 0.17	6.38
100 µM EDTA	N.D.	N.D.	N.D.
1000 mM K^+, 100 µM EDTA	N.D.	-41.29 ± 0.15	7.23
1 mM Mg^{2+}	-36.69 ± 1.00	-40.47 ± 0.16	7.09
4 mM Mg^{2+}	-40.58 ± 0.68	-42.54 ± 0.38	7.45
6 mM Mg^{2+}	-43.20 ± 1.52	-43.85 ± 0.23	7.68
8 mM Mg^{2+}	-46.18 ± 3.08	-43.94 ± 0.23	7.70
25 mM Mg^{2+}	-53.45 ± 1.21	-43.69 ± 0.26	7.65
50 mM Mg^{2+}	-52.36 ± 0.53	-44.60 ± 0.37	7.81
100 mM Mg^{2+}	-51.18 ± 1.68	-44.50 ± 0.24	7.80
10 mM K^+, 25 mM Mg^{2+}	N.D.	-43.85 ± 0.25	7.68
1 mM Ca^{2+}	-38.07 ± 0.21	-40.39 ± 0.19	7.08
4 mM Ca^{2+}	-40.62 ± 0.72	-41.56 ± 0.63	7.28
6 mM Ca^{2+}	-40.10 ± 2.45	-45.23 ± 0.26	7.93
8 mM Ca^{2+}	-43.12 ± 0.55	-44.84 ± 0.26	7.86
25 mM Ca^{2+}	-54.30 ± 4.50	-44.19 ± 0.28	7.74
50 mM Ca^{2+}	-53.80 ± 2.40	-44.29 ± 0.26	7.76
100 mM Ca^{2+}	-54.60 ± 4.70	-43.99 ± 0.23	7.71
10 mM K^+, 25 mM Ca^{2+}	N.D.	-44.14 ± 0.31	7.73

*imaging buffer contained 100 mM K^+ unless stated differently

Table S2: Cation-dependent d3'EBS1*-IBS1* docking/undocking as quantified by dwelltime analysis. Complementary cumulative probability distributions of dwell-times shown in Figs. 3 and S9 were fitted to single-, bi- or triexponential fit functions (m = 1 or 3, see Eqs. 9a and 9b).

Imaging buffer*	Normalized amplitudes a and decay constants τ (s), fastest to slowest											
	$a_{zero,1}$	$\tau_{zero,1}$	$a_{zero,2}$	$\tau_{zero,2}$	$a_{zero,3}$	$\tau_{zero,3}$	$a_{high,1}$	$\tau_{high,1}$	$a_{high,2}$	$\tau_{high,2}$	$a_{high,3}$	$\tau_{high,3}$
no additives	1.00	73.0	-	-	-	-	0.76	2.9	0.32	7.6	-	-
100 μM EDTA	static undocked											
1000 mM K^+, 100 μM EDTA	1.00	27.0	-	-	-	-	1.00	16.3	-	-	-	-
1 mM Mg^{2+}	0.50	16.7	0.50	36.9	-	-	0.38	2.8	0.62	18.8	-	-
4 mM Mg^{2+}	0.25	1.9	0.75	18.9	-	-	0.53	3.4	0.47	46.1	-	-
6 mM Mg^{2+}	0.75	7.7	0.25	43.6	-	-	0.17	0.3	0.47	3.8	0.36	33.6
8 mM Mg^{2+}	0.38	4.0	0.56	13.8	0.06	99.5	0.09	0.8	0.63	9.7	0.21	50.8
25 mM Mg^{2+}	0.22	0.4	0.50	5.3	0.28	28.6	0.55	8.0	0.45	25.9	-	-
50 mM Mg^{2+}	0.68	6.4	0.32	17.8	-	-	0.36	0.3	0.38	3.3	0.26	25.1
100 mM Mg^{2+}	1.00	14.7	-	-	-	-	0.30	0.7	0.43	6.3	0.27	44.9
10 mM K^+, 25 mM Mg^{2+}	1.00	53.6	-	-	-	-	0.49	14.5	0.51	93.6	-	-
1 mM Ca^{2+}	0.02	5.4	0.98	18.1	-	-	0.44	1.8	0.56	15.7	-	-
4 mM Ca^{2+}	N.D.						0.42	1.8	0.58	49.2	-	-
6 mM Ca^{2+}	0.28	2.3	0.60	8.0	0.12	31.6	0.76	2.1	0.05	40.2	-	-
8 mM Ca^{2+}	0.20	2.0	0.71	10.9	0.09	74.6	0.45	1.2	0.55	35.3	-	-
25 mM Ca^{2+}	0.59	19.5	0.41	54.5	-	-	0.52	2.2	0.40	19.9	0.08	75.8
50 mM Ca^{2+}	0.86	17.3	0.14	71.4	-	-	0.41	1.5	0.34	7.0	0.25	40.1
100 mM Ca^{2+}	1.0	29.0	-	-	-	-	0.29	0.4	0.39	4.6	0.32	33.7
10 mM K^+, 25 mM Ca^{2+}	N.D.											

*imaging buffer contained 100 mM K^+ unless stated differently

Table S3. Affinity constants of dynamic d3'EBS1*/IBS1* molecules: $K_{A,1}$, $K_{A,2}$, and $K_{A,3}$ and their corresponding amplitudes a_1, a_2, and a_3 in the presence of M^{2+} were obtained by fitting the experimental $P(K_{A,n})$ distributions to Eq. 17a. The last column lists the averaged log $K_{A,av}$: $\log \sum_{s=1}^{s\max} a_s \, 10^{\log K_{A,s}}$.

Imaging buffer*	log$K_{A,1}$	log$K_{A,2}$	log$K_{A,3}$	p	a_1	a_2	a_3	log$K_{A,av}$
no additives	5.96	-	-	1.6	1.00	-	-	5.96
1000 mM K^+, 100 µM EDTA	7.33	-	-	2.3	1.00	-	-	7.33
1 mM Mg^{2+}	5.70	6.75	7.48	2.1	0.07	0.29	0.64	7.32
4 mM Mg^{2+}	N.D.	N.D.	N.D.	N.D.	N.D.	N.D.	N.D.	N.D.
6 mM Mg^{2+}	6.39	7.39	8.48	2.2	0.26	0.39	0.35	8.06
8 mM Mg^{2+}	7.15	7.96	8.80	1.9	0.33	0.44	0.23	8.28
25 mM Mg^{2+}	6.20	7.37	8.12	2.8	0.23	0.50	0.27	7.68
50 mM Mg^{2+}	6.37	7.44	8.35	2.7	0.20	0.48	0.32	7.93
100 mM Mg^{2+}	6.62	7.49	8.29	2.7	0.21	0.36	0.38	7.93
10 mM K^+, 25 mM Mg^{2+}	7.07	8.10	-	1.7	0.59	0.41	-	7.77
1 mM Ca^{2+}	6.01	7.11	7.55	2.3	0.14	0. 46	0.38	7.29
4 mM Ca^{2+}	N.D.	N.D.	N.D.	N.D.	N.D.	N.D.	N.D.	N.D.
6 mM Ca^{2+}	6.79	7.99	8.80	2.3	0.29	0.43	0.28	8.34
8 mM Ca^{2+}	6.53	7.59	8.52	2.1	0.18	0.34	0.44	8.20
25 mM Ca^{2+}	5.81	6.89	7.91	2.1	0.14	0.49	0.37	7.53
50 mM Ca^{2+}	5.84	6.98	7.88	2.2	0.14	0.47	0.39	7.53
100 mM Ca^{2+}	6.14	7.23	7.93	2.4	0.20	0.39	0.41	7.62
10 mM K^+, 25 mM Ca^{2+}	6.71	8.02	-	1.6	0.65	0.35	-	7.60

*imaging buffer contained 100 mM K^+ unless stated differently

Table S4. Affinity constants of dynamic d3'EBS1*-IBS1* molecules: $K_{A,1}$, $K_{A,2}$, and $K_{A,3}$ and their corresponding amplitudes a_1, a_2, and a_3 in the presence of a constant concentration of 8 mM Mg^{2+} or Ca^{2+} and increasing IBS1* concentrations (Eq. 17b). The last column lists the averaged $\log K_{A,av}$: $\log \sum_{s=1}^{s\max} a_s \, 10^{\log K_s}$.

Imaging buffer	$\log K_{A,1}$	$\log K_{A,2}$	$\log K_{A,3}$	p	a_1	a_2	a_3	$\log K_{A,av}$
1 nM IBS1*, 8 mM Mg^{2+}	5.03	7.12	8.01	1.9	0.12	0.29	0.59	7.81
1 nM IBS1*, 8 mM Ca^{2+}	4.44	7.15	7.78	1.9	0.17	0.32	0.51	7.54
5 nM IBS1*, 8 mM Mg^{2+}	6.46	7.75	8.82	1.9	0.29	0.27	0.44	8.48
5 nM IBS1*, 8 mM Ca^{2+}	4.47	7.45	8.21	1.9	0.09	0.41	0.50	7.97
10 nM IBS1*, 8 mM Mg^{2+}	4.78	7.29	7.96	1.9	0.07	0.35	0.58	7.78
10 nM IBS1*, 8 mM Ca^{2+}	4.35	7.56	8.28	1.9	0.11	0.30	0.59	8.09
25 nM IBS1*, 8 mM Mg^{2+}	4.62	7.34	8.28	1.9	0.18	0.13	0.69	8.13
25 nM IBS1*, 8 mM Ca^{2+}	4.54	8.18	8.84	1.9	0.11	0.49	0.40	8.55
40 nM IBS1*, 8 mM Mg^{2+}	5.28	7.85	8.77	1.9	0.13	0.42	0.45	8.47
40 nM IBS1*, 8 mM Ca^{2+}	5.22	7.97	8.89	1.9	0.16	0.43	0.41	8.55

*imaging buffer consistently contained 100 mM K^+

Table S5. Solutions used throughout smFRET and UV thermal melting experiments.

Solution name	Composition
T50 buffer	50 mM Tris-HCl, 50 mM NaCl, pH 7.50
BSA-biotin solution	1 mg/mL , dissolved in T50 buffer
Streptavidin solution	50 µg/mL, dissolved in T50 buffer
Standard buffer	50 mM MOPS, 100 K^+, Ca^{2+} or Mg^{2+} at varying concentration, pH 6.90
EBS1* solution	10 pM, dissolved in standard buffer
100x oxygen scavenger solution (OSS)	80 µL T50 buffer, 2170 U/mL catalase, 165 U/mL glucose oxidase
Trolox stock solution	Trolox in standard buffer, pH 6.90
Reaction buffer	25 nM IBS1*, 1 mM Trolox (dilution from stock), 1x OSS (dilution from stock), 1 % (w/v) D-glucose, dissolved in standard buffer